Characterization of Nonradiative Recombination Centers in GaPN Alloys by Two-Wavelength Excited Photoluminescence

(二波長励起フォトルミネッセンスによるGaPN混晶における非発光再結合中心の評価)

A dissertation submitted to the Graduate School of Science and Engineering of Saitama University in partial fulfillment of the requirements for the degree of Doctor of Philosophy

By

Sanjida Ferdous

Student ID: 18DS153

Written under the supervision of

Professor Hiroyuki Yaguchi

Saitama University, Japan

September 2021

Copyright © 2021 by

Sanjida Ferdous

Dedicated to my daughter

Sidrat Muntaha

ABSTRACT

Among renewable energies, power generation using solar cells is drawing attention. However, the problem with solar power generation lies in its generation cost. It is essential to reduce the power generation cost of renewable energy, when making it the main power source. Higher efficiency of solar cells has been desired with the aim of reducing the cost of photovoltaic power generation. One of the attempts to achieve high efficiency is an intermediate band solar cell (IBSC). Although there is a rapid technological progress of growth technique, the performance of IBSCs shows less than the expectation partly due to the presence of deep level defects which originate from point defects, dislocations and so on. The deep level defects which are located below the conduction band minima or intermediate band act as nonradiative recombination (NRR) centers. It is crucial to reduce the NRR centers to improve photoconversion efficiency of IBSCs.

GaPN alloys can be a material candidate for efficient IBSCs due to the cascade excitation of photo-generated carriers via the IB in addition to the direct excitation of carriers from the valence band (VB) to the conduction band (CB). Doping with nitrogen into GaP can lead to an extremely large bandgap bowing and demonstrate quasi-direct bandgap behavior. Isolated N atoms at a low concentration induces highly localized isoelectronic traps, and the formation of the impurity band occurs sequentially by spatial and energetic overlap among different isoelectronic trap centers with increasing N concentration.

In this research work, a purely optical and non-destructive technique of two-wavelength excited photoluminescence (TWEPL) method was used for the detection and characterization of NRR centers. We have constructed a schematic energy diagram of NRR processes among CB, IB and VB considering the impact of the irradiation of an intermittent below-gap excitation (BGE) light on the IB PL under two kinds of above-gap excitation (AGE) light (CB or IB excitation). By combining experimental data of time-resolved photoluminescence (TRPL), solving the rate equations based on the postulated energy diagram and fitting the results with experimental data of TWEPL, the relative contributions of NRR parameters are evaluated.

The key contributions of this work are as follows:

The GaPN sample was grown by metalorganic chemical vapor deposition (MOCVD). A 300 nm-thick GaP buffer layer and a 500 nm-thick $GaP_{1-x}N_x$ ($x = 0.105\%$) were grown in sequence on a 400 μm-thick sulfur doped GaP substrate with an orientation of (100). Trimethylgallium, phosphine, and dimethylhydrazine were used as Ga, P, and N sources, respectively. The sample was excited by two types of AGE light sources: 2.33 eV (532 nm) for IB and 3.49 eV (355 nm) for CB excitation. Another intermittent BGE light was superposed over AGE at the same point of the sample. The NRR level was detected and evaluated by measuring the change in the PL intensity with the irradiation of BGE. Five types of lasers (0.81, 0.93, 1.17, 1.27, 1.46 eV) were used as the BGE light sources. The temperature effect due to BGE irradiation on the sample was eliminated by immersing it in liquid N_2. Depending on the excitation energies of BGE, different contribution of one-level model and two-level model took place for CB and IB excitation. The effect of BGE energies depends also on the AGE excitation power density through a shift of Fermi level in the forbidden energy gap. These results are successfully interpreted by the distribution of NRR centers and NRR processes among CB, IB and VB. Finally, the NRR parameters were evaluated by rate equation analysis. The rate equation analysis has been performed to justify the phenomenological recombination model combining the result of TRPL measurements.

Similarly, the carrier recombination model of $GaP_{1-x}N_x$ ($x = 0.56$ and 0.75%) samples are interpreted from the experimental results of TWEPL and the NRR parameters are evaluated by TRPL measurements and rate equation analysis based on the recombination model.

It was observed from the experimental results that with increasing N concentration, the PL spectrum of $GaP_{1-x}N_x$ transforms from superposition of discrete peaks to a broader PL band corresponding to the formation of IB. The increase in the N concentration of GaPN alloy causes a shift of the IB emission toward lower energies. When BGE light was irradiated on $GaP_{1-x}N_x$ ($x = 0.56$ and 0.75%) samples, the PL intensity increased for all five BGE, whereas in the sample with a N concentration of 0.105%, such a clear tendency was not shown for all BGE lights, and different BGE energy dependence was observed. This is

because the energy distribution of NRR centers is different in each sample, and different carrier recombination processes can be considered for each sample. The evaluated NRR parameters by TRPL measurements and rate equation analysis of three samples shows that the defect density of $GaP_{1-x}N_x$ ($x = 0.56\%$) sample is the lowest among three samples. The experimental results shows that $GaP_{1-x}N_x$ ($x = 0.56\%$) sample has the highest emission efficiency with a low NRR density.

It was found from the evaluation that the energy distribution of the carrier recombination process via IB was different due to a slight change in N concentration. For actual application of GaPN alloy for IBSC, the Fermi level should be very near or inside the IB. The reduction of the defect density inside the forbidden gap is also important to raise the Fermi level up to IB. This work also implies that the combination of TRPL results with TWEPL is important to improve the accuracy toward quantitative determination of NRR parameters. However, more samples with higher N concentrations should be investigated to find the best condition of GaPN alloys for the application of IBSC. Considering the detection sensitivity, merit of non-contacting and non-destructive measurement, the way of utilizing the IB luminescence as a probe of characterizing defect levels is beneficial not only for GaPN but also InAs/GaAs, N δ-doped GaAs superlattice and other IBSC materials.

ACKNOWLEDGEMENTS

Firstly, I would like to express my special appreciation and thanks from heart to my supervisor Professor Hiroyuki Yaguchi and former supervisor Professor Norihiko Kamata for their valuable and scholastic guidance, consistent encouragement, amicable disposition, and invaluable discussion throughout the research work. I am very much fortunate to get a chance to have two supervisors like you and grateful to them for allowing me to do research work under their kind supervision.

I would also like to express my gratitude to the rest of my thesis committee: Professor Masamichi Sakai, Professor Zentaro Honda and Professor Shuhei Yagi for their valuable advice and guidance during my PhD study. I am also very much grateful to Professor Hiroyuki Yaguchi and Professor Shuhei Yagi for helpful discussion and providing samples.

I consider myself to be very fortunate for getting help from Dr. Ismail Hossain, Dr. Md Julkarnain and Professor A. Z. M. Touhidul Islam. I am very much grateful to them for their guidance, discussion, and suggestions during my study. Without their kind help and guidance, it was impossible for me to understand and accustom with new experimental setup and system very quickly.

I want to thank Ms. Chika Negishi for her valuable support to learn and familiar with the experiment system. I want to thank Mr. Hiroki Iwai for his valuable support during my experiment. I would like to express my gratitude to all my lab. members for their support and all the fun we have had in past three years.

Special thank goes to Ministry of Education, Culture, Sports, Science, and Technology (MEXT) Japan for providing the scholarship.

Finally, I would like to convey my deepest gratitude to my beloved parents and all my family members especially my beloved husband who has sacrificed a lot last three years. Your unconditional support and patience have helped me to be successful in my endeavors. You have made my life more meaningful and joyful.

List of Publication

Journal Paper

1. “Detection of Nonradiative Recombination Centers in GaPN (N:0.105%) by Below-Gap Excitation Light”, published in “Physica Status Solidi (b) Vol. 257, No. 2, pp. 1550-1555 (2020)”, Authorized by **Sanjida Ferdous***, Norihiko Kamata, Shuhei Yagi and Hiroyuki Yaguchi.

2. “Detection of Nonradiative Recombination Centers in GaPN by Combining Two-Wavelength Excited Photoluminescence and Time-Resolved Photoluminescence”, published in Physica Status Solidi (b) 2021, Authorized by **Sanjida Ferdous***, Hiroki Iwai, Norihiko Kamata, Hiroyuki Yaguchi and Shuhei Yagi.

Conference Presentation

1. **Sanjida Ferdous,** Chika Negishi, Norihiko Kamata, Shuhei Yagi and Hiroyuki Yaguchi**,** “*Detection of Nonradiative Recombination Centers in GaPN (N:0.105%) by Below-Gap Excitation Light Without Temperature Effect”,* International Symposium on Compound Semiconductor Physics (ISCS 2019) 46th, TuP-D-10, May 19-23, 2019, Nara, Japan.

VITAE

1993	Born, Naogaon, Bangladesh
2015	B. Sc. in Applied Physics and Electronic Engineering, University of Rajshahi, Bangladesh
2017	M. Sc. in Applied Physics and Electronic Engineering, University of Rajshahi, Bangladesh
2018-2021	Doctoral Candidate, Saitama University, Japan

CONTENTS

ABSTRACT i
ACKNOWLEDGEMENTS iv
LIST OF PUBLICATION v
VITA vi
CONTENTS vii
LIST OF TABLES x
LIST OF FIGURES xi
LIST OF ABBREVIATIONS xiv
CHAPTER 1 1
INTRODUCTION 1
1.1 Motivation 1
1.2 Objectives 2
1.3 Organization of the Thesis 3
CHAPTER 2 5
BACKGROUND 5
2.1 Intermediate Band Solar Cell and Its Candidates 5
2.2 Basic Properties of GaPN Alloy 5
2.3 Isoelectronic Trap in GaP Crystal 7
2.4 Crystal Growth Technology for GaPN Alloy Semiconductors 9
2.5 Energy band structure of GaPN alloy semiconductor 10
2.6 Shockley-Read-Hall (SRH) Recombination Theory 12
2.7 Two-wavelength Excited Photoluminescence (TWEPL): A tool for non-radiative recombination centers characterization 16
CHAPTER-3 18
EXPERIMENTAL DETAILS 18
3.1 Photoluminescence 18
3.2 Two-wavelength Excited Photoluminescence 18
3.3 Sample Structure 21
CHAPTER 4 23

CHARACTERIZATION OF NONRADIATIVE RECOMBINATION CENTERS IN GaPN(0.105%) **23**

4.1 Introduction **23**

4.2 Results and Discussion **23**

4.2.1 Temperature Dependence 23

4.2.2 PL Intensity 25

4.2.3 Characterization of NRR centers 27

4.2.4 Time-resolved PL Measurement and Determination of Trap Parameters by Rate Equation Analysis 32

4.3 Conclusion **37**

CHAPTER 5 .... **38**

CHARACTERIZATION OF NONRADIATIVE RECOMBINATION CENTERS IN GaPN(0.56%) **38**

5.1 Introduction **38**

5.2 Results and Discussion **38**

5.2.1 PL Intensity 38

5.2.2 BGE Dependence of the PL Intensity 40

5.2.3 Characterizations of NRR centers 42

5.2.4 Time-resolved PL Measurement and Determination of Trap Parameters by Rate Equation Analysis 43

5.3 Conclusion **48**

CHAPTER 6 .... **49**

CHARACTERIZATION OF NONRADIATIVE RECOMBINATION CENTERS IN GaPN(0.75%) **49**

6.1 Introduction **49**

6.2 Results and Discussion **49**

6.2.1 PL Intensity 49

6.2.2 BGE Dependence of the PL Intensity 51

6.2.3 Characterizations of NRR centers 53

6.2.4 Time-resolved PL Measurement and Determination of Trap Parameters by Rate Equation Analysis 55

6.3 Conclusion **60**

CHAPTER 7 .... **61**

COMPARISON OF NONRADIATIVE RECOMBINATION PARAMETERS OF GaPN SAMPLES WITH N CONCENTRATION OF 0.105. 0.56 AND 0.75%.........61

7.1 Introduction.........61

7.2 Results and Discussion.........61

7.2.1 N Concentration Dependence of PL Intensity.........61

7.2.2 BGE Effect.........65

7.2.3 Time-resolved PL Measurement.........65

7.2.4 Comparison of NRR parameters.........66

7.3 Conclusion.........68

CHAPTER 8.........69

SUMMARY AND FUTURE DIRECTIONS.........69

8.1 Summary.........69

8.2 Future Directions.........71

APPENDIX.........73

A.1 Calibration of different BGE sources output power.........73

A.2 Beam parameters of different laser sources.........75

REFERENCES.........76

LIST OF TABLES

Table 4.1. PL decay time of $GaP_{1-x}N_x$ (x=0.105%) for CB excitasion……………………..**34**

Table 4.2. Values of C_{p1} and N_{t1} for $GaP_{1-x}N_x$ (x=0.105%) determined by TRPL measurement. **..35**

Table 4.3. Trap parameters of the dominant NRR1 center for IB excitation.**....................35**

Table 5.1. PL decay time of $GaP_{1-x}N_x$ (x=0.56%) for CB excitasion.**................................44**

Table 5.2. Values of C_{p1} and N_{t1} for $GaP_{1-x}N_x$ (x=0.56%) determined by TRPL measurement. **..44**

Table 5.3. Trap parameters of the dominant NRR1 center for IB and CB excitation. **......45**

Table 6.1. PL decay time of $GaP_{1-x}N_x$ (x=0.75%) for CB excitasion. **..............................55**

Table 6.2. Values of C_{p1} and N_{t1} for $GaP_{1-x}N_x$ (x=0.75%) determined by TRPL measurement. **..56**

Table 6.3. Trap parameters of the dominant NRR1 center for IB and CB excitation. **......57**

Table 7.1. PL decay time for CB excitasion. **..66**

Table 7.2 Comparison of the results of GaPN samples obtained by the rate equation analysis.**...68**

Table A.1 Beam parameters of different lasers……………………………………….….**75**

LIST OF FIGURES

Figure 2.1 Photoluminescence spectrum of GaP:N (nitrogen concentration:10^{19} cm^{-3})....6

Figure 2.2 Figure 2.2 Band Structure of GaP at room temperature……….…...................7

Figure 2.3 Formation of isoelectronic trap by isolated nitrogen atom / nitrogen atom pair……………………………………………………………………8

Figure 2.4 Energy level of electron trap such as nitrogen in GaP crystal…………………9

Figure 2.5 Crystal structure of GaP and GaN and bandgap energy E_g at 300 K………..…10

Figure 2.6 GaPN alloy photoluminescence spectrum………………………………….....11

Figure 2.7 Band structure of GaPN alloy (nitrogen concentration 0.8%) shown by first-principles calculation…………………………………………………………………12

Figure 2.8 The basic processes involved in Shockley-Read-Hall recombination statistics...12

Figure 3.1 (a) One level model which explains the enhancement of the PL intensity, (b) Two levels model used for the illustration of the PL intensity quenching. 19

Figure 3.2 Experimental setup for TWEPL measurement (a) metal cryostat (b) glass cryostat...20

Figure 3.3 Schematic diagram of $GaP_{1-x}N_x$ sample structures……………………….…..22

Figure 4.1 (a) Temperature-dependent PL spectra (b) Normalized PL spectra with increasing temperature (c) The intensity of 5 dominant peaks in Figure (a) as a function of temperature. 25

Figure 4.2 AGE power density dependent PL intensity for a) CB excitation and b) IB excitation. c) Integrated PL intensity for IB and CB excitation. 27

Figure 4.3 I_N values as a function of BGE photon number density for CB excitation with AGE (a) 20.04 Wcm^{-2} and (b) 3.28 Wcm^{-2}...28

Figure 4.4 I_N values as a function of BGE photon number density for IB excitation with AGE (a) 31.08 Wcm^{-2} and (b) 5.94 Wcm^{-2}...30

Figure 4.5 Schematic energy diagram of NRR processes in $GaP_{1-x}N_x$ (x=0.105%) alloy for high excitation energy of AGE……………………………………………….........31

Figure 4.6 Schematic energy diagram of NRR processes in $GaP_{1-x}N_x$ (x=0.105%) alloy for low excitation energy of AGE…………………………………………………….32

Figure 4.7 PL decay profile of $GaP_{1-x}N_x$ (x=0.105%) with fitting curve under CB excitation………………………………………………………………………...34

Figure 4.8 (a) Variation of I_N values as a function of G_2 and (b) Variation of I_N values as a function of G_1 at 77 K for 1.46 eV BGE for IB excitation. **36**

Figure 5.1 AGE power density dependent PL intensity for a) CB excitation and b) IB excitation. c) Integrated PL intensity for IB and CB excitation. **40**

Figure 5.2 Variation of I_N values as a function of BGE photon number density for (a) IB and (b) CB excitation. **41**

Figure 5.3 Schematic energy diagram of NRR processes in $GaP_{1-x}N_x$ (x=0.56%) alloy**.** The spectrum of IB-PL (colored by orange) indicates the position of the IB. **43**

Figure 5.4 PL decay profile of $GaP_{1-x}N_x$ (x=0.56%) with fitting curve under CB excitation. **44**

Figure 5.5 (a) Variation of I_N values as a function of G_2 and (b) Variation of I_N values as a function of G_1 at 77 K for 1.46 eV BGE for IB excitation. **46**

Figure 5.6 (a) Variation of I_N values as a function of G_2 and (b) Variation of I_N values as a function of G_1 at 77 K for 1.46 eV BGE for CB excitation. **48**

Figure 6.1 AGE power density dependent PL intensity for a) CB excitation and b) IB excitation. c) Integrated PL intensity for IB and CB excitation. **51**

Figure 6.2 Variation of I_N values as a function of BGE photon number density for (a) IB and (b) CB excitation. **52**

Figure 6.3 Schematic energy diagram of NRR processes $GaP_{1-x}N_x$ (x=0.75%) in alloy. The spectrum of IB-PL (colored by orange) indicates the position of the IB. **54**

Figure 6.4 PL decay profile of $GaP_{1-x}N_x$ (x=0.75%) with fitting curve under CB excitation. **56**

Figure 6.5 (a) Variation of I_N and f_{t1} values as a function of G_2 and (b) Variation of I_N values as a function of G_1 at 77 K for 0.93 eV BGE for IB excitation. **58**

Figure 6.6 (a) Variation of I_N and f_{t1} values as a function of G_2 and (b) Variation of I_N values as a function of G_1 at 77 K for 1.27 eV BGE for CB excitation. **60**

Figure 7.1 PL spectra of $GaP_{1-x}N_x$ samples (x= 0.105, 0.56 and 0.75%) at 77 K. **62**

Figure 7.2 PL intensity for IB and CB excitation for (a) GaPN (0.105%), (b) GaPN (0.56%), and (c) GaPN (0.75%) samples. **64**

Figure 7.3 Integrated PL intensity for IB and CB excitation with AGE photon number density. **64**

Figure 7.4 PL decay profile of $GaP_{1-x}N_x$ (x=0.105%, 0.56%, and 0.75%) samples with fitting curve under CB excitation........**66**

Figure 7.5 Schematic energy band diagram of three samples. **67**

Figure A.1 Calibration of the 850 nm (1.46 eV) laser. **73**

Figure A.2 Calibration of the 980 nm (1.27 eV) laser. **73**

Figure A.3 Calibration of the 1064 nm (1.17 eV) laser. **74**
Figure A.4 Calibration of the 1550 nm (0.81 eV) laser. **74**

LIST OF ABBREVIATIONS

AGE	Above Gap Excitation
BGE	Below Gap Excitation
CBE	Conduction Band Edge
DLOS	Deep Level Optical Spectroscopy
DLTS	Deep Level Transient Spectroscopy
DL	Defect Level
IBSC	Intermediate Band Solar Cell
IB	Intermediate Band
IQE	Internal Quantum Efficiency
LD	Laser Diode
LED	Light Emitting Diode
MBE	Molecular Beam Epitaxy
MQW	Multiple Quantum Well
MOVPE	Metalorganic Vapor Phase Epitaxy
Nd: YAG	Neodymium-doped Yttrium Aluminum Garnet
NRR	Nonradiative Recombination
PL	Photoluminescence
QW	Quantum Well
QD	Quantum Dot
SRH	Shockley-Read-Hall
TWEPL	Two-wavelength Excited Photoluminescence

CHAPTER 1
INTRODUCTION

1.1Motivation

Energy is an indispensable part of today's life. The industrial revolution of most countries across the world has become dominated by fossil fuels. This has a major implication for the global climate as well as human health. Three-quarters of global greenhouse gas emissions result from the burning of fossil fuels for energy. To reduce CO_2 emissions, the world needs to rapidly shift towards low-carbon sources of energy. Renewable energy will play a vital role in the decarbonization of our energy systems in the coming decades.

Among renewable energies, power generation using solar cells is drawing attention. Solar field photovoltaic power generation compared to power generation using fossil fuels, the greenhouse gas discharge is small as well as it is safe and powerful. However, the problem with solar power generation lies in its generation cost. It is essential to reduce the power generation cost of renewable energy, when making it the main power source. Higher efficiency of solar cells has been desired with the aim of reducing the cost of photovoltaic power generation. One of the attempts to achieve high efficiency is an intermediate band solar cell (IBSC). The IBSC has a structure in which a band is provided in the middle of the band gap of the single-junction solar cell, and it is possible to realize high conversion efficiency by increasing the photocurrent via the IB.

The use of a discrete electronic energy level within the band gap of semiconductor materials which drives sub-bandgap photon absorption was previously reported by Wolf[1] in 1960. Barnham and Duggan proposed the use of multiple quantum well solar cells to absorb sub-bandgap photons[2]. The concept of IBSC was firstly proposed in 1997 by Luque and Marti then later explained thermodynamic consistency of sub-band gap photon absorption [3,4]. The limiting efficiency of solar cells with three-bands (63.2%) and four-bands (71.7%) has been calculated by Brown, Green and Corkish [5]. By tailoring the electronic band structure of mismatched alloy or hetero-structures, the existence of three electronically isolated energy bands have been represented in IBSC structures by

researchers. Highly mismatched alloys are the class semiconductor comprising isoelectronic elements with different atom size, ionicity and electronegativity [6-8].

Although there is a rapid technological progress of growth technique, the performance of IBSC shows less than the expectation due to present of deep level defects. These deep level defects are originated from the lattice mismatched, point defect etc. The deep level defects which are located below conduction band (CB) minima or intermediate band (IB) act as nonradiative recombination (NRR) centers. The elimination of NRR centers is the main concern of the crystal grower. It is crucial to reduce the densities of NRR centers to improve photoconversion efficiency of IBSC materials. Furthermore, the efficiency and reliability enhancement of IBSCs by reducing NRR centers requires an in-depth understanding of the basic mechanism of as grown defects and imperfections in these materials. Such advancement requires a way to identify NRR levels in IBSC materials conclusively, evaluate their influence on relevant material properties, and assign them to their physical origin. Thus, the study of NRR centers is likely to remain an important and active research thrust for realization of high IBSC technologies.

1.2 Objectives

Gallium phosphide (GaP) causes an interest of its application as a material for optoelectronics and photovoltaic devices. Adding dopants in GaP can lead to profound effect on electronic properties and allow widely extended band gap engineering.[7-9] Doping with nitrogen (N) as isoelectronic impurity can increase the functionality of GaP based materials by leading to an extremely large bandgap bowing and demonstrating quasi-direct bandgap behavior.[10-17] Isolated N at a low content induces highly localized isoelectronic traps, and the formation of the impurity band occurs sequentially by special and energetic overlap among different NN_i centers with increasing the N doping level.[18-22] The impurity band in between valence band (VB) and CB is IB and it implies that GaPN alloys can be a material candidate for efficient IBSCs due to the cascade excitation of photo-generated carriers via the IB in addition to the direct excitation of carriers from VB to CB. The Basic principles of operation were originally described by Luque and Marti [3,23].

However, many parts of the characteristics of electron traps and IBs of GaPN alloy have not been clarified yet. The search for its basic physical properties is indispensable for practical use and further development. GaP (zincblende) and GaN (wurtzite) are different in crystal structure and lattice constant, which arises difficulty to grow high quality epitaxial layer of GaPN alloy. Lack of lattice matching brings difficulties in reducing densities of defect states, which act as NRR centers in GaPN alloys.[24-27] Different research works suggest that the GaPN layer contains deep-level defects which are associated with nitrogen interstitials, vacancies, and N-related defects such as N-N pairs, N clusters and N-related complexes.[28-29] The actual efficiency of IBSCs is determined by the competition of cascade photo-excitation rate via the IB, and other radiative and NRR rates with these NRR centers. For the development of GaPN alloy based IBSCs, it is indispensable to understand the formation and properties of NRR centers and eliminate them during growth process.

In this research work, a purely optical and non-destructive technique of Two-Wavelength Excited Photoluminescence (TWEPL) method was used for the detection and characterization of NRR centers. With the irradiation of an intermittent below-gap excitation (BGE) light and investigating its impact on the IB photoluminescence under two kinds of above-gap excitation (AGE) light (CB or IB excitation), we have interpreted a schematic energy diagram of NRR processes among CB, IB and VB. By combining experimental data of TRPL, solving the rate equations based on the postulated energy diagram and fitting the results with experimental data of TWEPL, the relative contribution of NRR parameters are evaluated.

1.3 Organization of the Thesis

The motivation and objectives of this research work are introduced in chapter 1. The layout of this dissertation also presented here.

Chapter 2 deals with the background of this work. The basic properties of materials with the fundamental of GaPN briefly explained there. A survey prospect and application of TWEPL is also presented in this chapter.

In chapter 3, detailed experimental setup of conventional photoluminescence and two wavelength excited photoluminescence is demonstrated.

The results of GaPN (0.105%) sample are presented in chapter 4. Recombination model has been proposed based on the experimental evidence. The effect of nitrogen concentration on the formation of NRR centers has been explained. Defect related parameters have been estimated by model consideration and fitting the result with experiment.

The results of GaPN (0.56%) sample are presented in chapter 5. A recombination model has been proposed based on the experimental results. The rate equation an analysis has been performed to justify the phenomenological recombination model combining the result of time-resolved PL measurement.

In chapter 6, the NRR centers of GaPN (0.75%) samples have been investigated by TWEPL. The change of PL intensity of the sample after irradiation of BGE can be interpreted by one level model. By combining results of time-resolved PL measurement and rate equation analysis the NRR parameters have been estimated from the recombination model.

In chapter 7 a comparative study between the experimental results of GaPN samples with three different N concentrations have been reported.

Finally, the summary of this research work and guideline for future research is presented in chapter 8.

CHAPTER 2
BACKGROUND

2.1 Intermediate Band Solar Cell and Its Candidates

Intermediate band solar cell (IBSC) introduces an intermediate band (IB) energy level in between the VB and CB. Theoretically, introducing an IB allows two photons with energy less than the bandgap to excite an electron from the VB to the CB. This increases the induced photocurrent and thereby efficiency. The concept of IBSC was firstly proposed in 1997 by Luque and Marti then later explained thermodynamic consistency of sub-band gap photon absorption [3,4]. In the IBSC, it is said that sunlight with energy that causes transmission loss in the conventional solar cell can be used through the intermediate band. This feature improves efficiency from 40.7% up to 63.2%. However, the performance of IBSCs is reduced by the presence of NRR centers. Therefore, research on NRR centers is necessary for using semiconductors with IBs for IBSCs.

IBSC materials such as InAs/GaAs, GaAsN alloys, GaPN and GaAs:N δ-doped superlattice are promising for the high efficiency solar cell due to the cascade excitation of photo-generated carriers by the below-gap photons and direct excitation of carriers from VB to CB. In these material structures, the electron can be excited from the VB to the IB and then IB to CB. Two different research directions are involved to seek the proper IBSC materials. One of them is the dilute nitride alloy or SL structure and another research direction is the formation of IB below the CB by the fabrication of quantum dots (QD) inside the host semiconductor.

2.2 Basic Properties of GaPN Alloy

Since the III-V-N alloy semiconductor has the characteristic property of a huge bandgap bowing in which the bandgap decreases remarkably as the nitrogen concentration increases. At a low nitrogen concentration, an optical device that is difficult to realize with a conventional material system is manufactured. It is expected as a possible semiconductor material.

Research on GaPN alloy semiconductors has been carried out since the 1960s and has been carried out earlier than research on GaAsN alloys, which are the same III-V-N alloy semiconductors. It has been reported that GaPN alloys also have nitrogen binding levels that are not found in ordinary mixed crystals. Several studies are already available on the N doped GaP system based on photoluminescence (PL), PL excitation (PLE) spectroscopy,[18] temperature dependent PL spectroscopy,[30-35] and time-resolved PL studies.[36-39] Figure 2.1 shows the photoluminescence spectrum of nitrogen-doped GaP.[19]

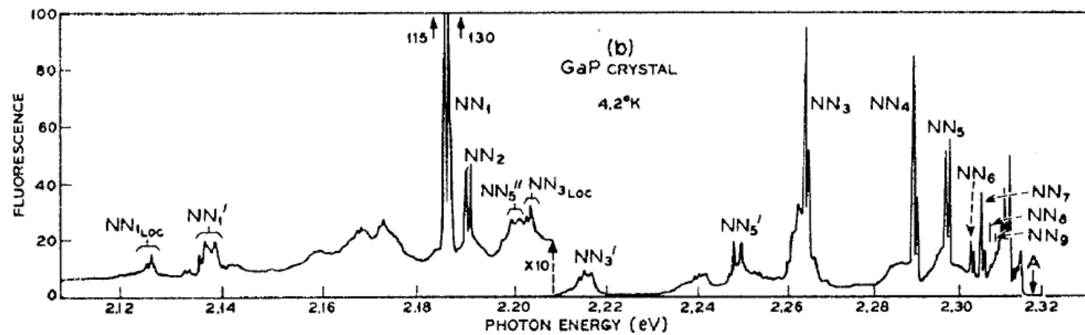

Figure 2.1 Photoluminescence spectrum of GaP: N (nitrogen concentration: 10^{19} cm^{-3}).

Since GaP is an indirect transition type semiconductor, it has an extremely low luminous efficiency, but it has a feature that the luminous efficiency is improved by adding a very small amount of nitrogen. This is because the nitrogen atom has a much higher electronegativity than other group V atoms, and an isoelectronic trap is formed around the nitrogen atom by substituting it with a phosphorus atom to attract electrons. Nitrogen introduced into GaP during growth will almost certainly substitute isoelectronically for a phosphorus atom.[40] An isolated nitrogen atom evidently binds an exciton. Two nitrogen atoms close together might be expected to bind an exciton more tightly. As the distance between the members of a pair increases the exciton will be bound with an energy that becomes increasingly close to that for the isolated atom. Thus, a model may be tried in which the lowest energy line observed, NN_1 is ascribed to a nitrogen atom on a phosphorus site with another nitrogen atom on the nearest shell of phosphorus sites. NN_2 then has a nitrogen on the next nearest shell of phosphorus sites, and so on. So, with increasing N, a variety of NN pair lines with the spacing index i (NN_i) have been observed by

photoluminescence (PL) spectrum in addition to reduction of the fundamental energy gap of GaP. [41, 42] Their wave functions overlap with a further increase in N concentration to form delocalized IB between the CB and VB of $GaP_{1-x}N_x$. The CB edge originates from the N isoelectronic level but is expanded continuously toward low energy side due to IB.[43,44] As the energy difference between CB and VB can be 2.3 eV and that between CB and IB be 0.8 eV, $GaP_{1-x}N_x$ is considered to be a promising candidate for the IBSCs with an improved efficiency. The development of IBSCs seeks to enhance the conversion efficiency of solar cells [3, 45, 46].

2.3 Isoelectronic Trap in GaP Crystal

When an impurity atom having the same valence electron configuration as the atom constituting the crystal is added to the parent crystal, an energy level due to excitons bound to the impurity appears in the band gap of the mother crystal. The electronic state strongly localized around impurities in the real space spreads in the wave number space, and as a result, the emission recombination probability can be increased even in the indirect transition type semiconductor as in the direct transition type semiconductor.

Since GaP is an indirect transition type semiconductor whose bottom at the X point of the CB. The band structure of GaP is shown in Figure 2.2.[47]

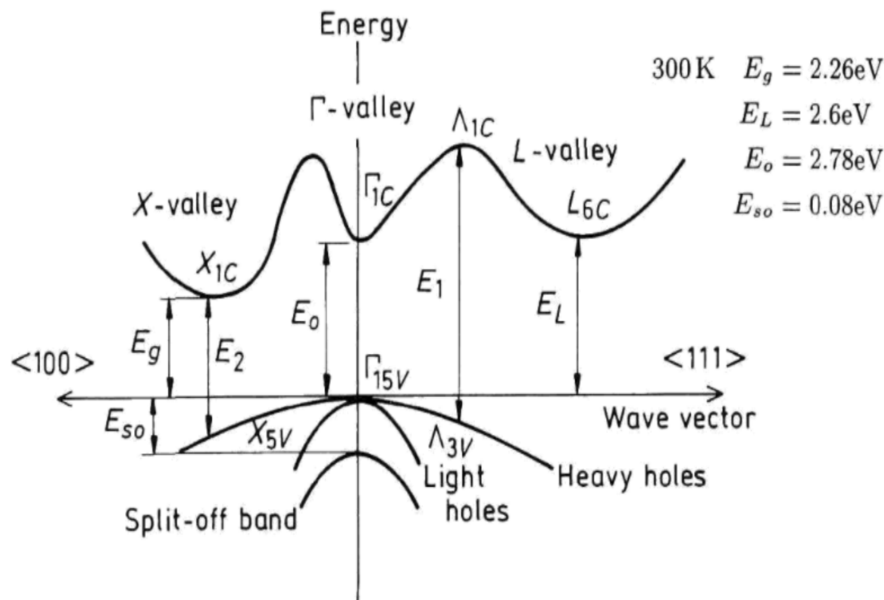

Figure 2.2 Band Structure of GaP at room temperature.

Here, it is assumed that a nitrogen atom is added to GaP. Since the electronegativity of a nitrogen atom is higher than that of a phosphorus atom, the nitrogen atom has a property of easily capturing an electron. This is called an isoelectronic trap. This difference in electronegativity, unlike the Coulomb force, is only felt when the electron is very close to the nitrogen atom. The Coulomb force, for example, the wave function of ionized impurities spreads as much as 3-5 nm, while the distance affected by the difference in electronegativity is said to be only about 0.1-0.2 nm. Therefore, the electrons trapped by the nitrogen atom exist only in the immediate vicinity of the nitrogen atom.

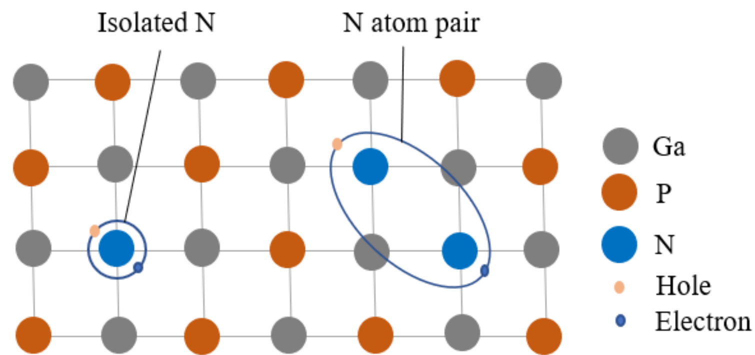

Figure 2.3 Formation of isoelectronic trap by isolated nitrogen atom / nitrogen atom pair.

In this way, when an electron is confined in an extremely narrow space, the momentum of the electron is accompanied by Heisenberg's uncertainty principle ($\Delta x \cdot \Delta p \cong h$, the product of position and momentum is accompanied by an uncertainty of about h) can no longer be determined accurately. Therefore, the electron wavefunction spreads over a wide range in k-space. Among the electrons captured by the nitrogen atom, the electron having a crystal momentum near $k = 0$ undergoes a direct transition type exciton recombination with the hole in the VB. In other words, since the wave function of an electron is strongly bound to a nitrogen atom and extends to the vicinity of the Γ point at k = 0 in the wavenumber space by the uncertainty principle, it increases the emission recombination probability like a direct transition type semiconductor. It can be done (Fig. 2.4). In the process of recombination of excitons bound to electron traps such as nitrogen in GaP crystals, green light emission with energy close to the band gap is obtained. This has

attracted practical attention, and GaPN is currently widely used as a material for green light emitting diodes.

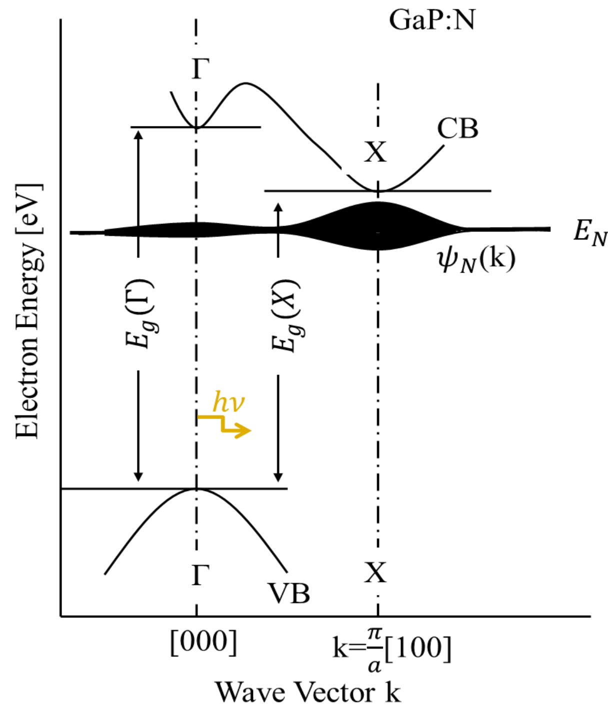

Figure 2.4 Energy band structure of nitrogen doped GaP crystal.

2.4 Crystal Growth Technology for GaPN Alloy Semiconductors

GaP and GaN have different crystal structures and different lattice constants (Figure 2.4). Due to this difference in miscibility, it becomes difficult to produce a high-quality epitaxial GaPN mixed crystal layer.

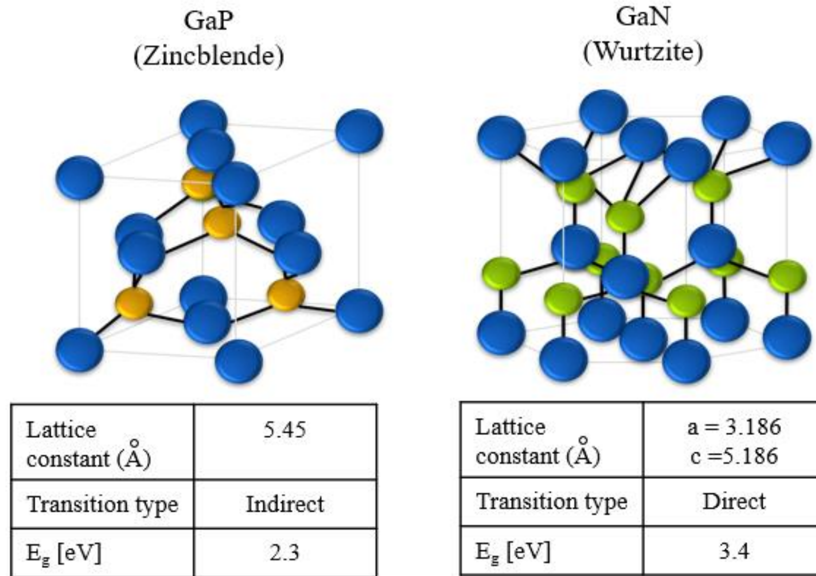

Lattice constant (Å)	5.45
Transition type	Indirect
E_g [eV]	2.3

Lattice constant (Å)	a = 3.186 c =5.186
Transition type	Direct
E_g [eV]	3.4

Figure 2.5 Crystal structure of GaP and GaN and bandgap energy E_g at 300 K.

In early studies, liquid phase epitaxy and chloride vapor deposition methods have been used to grow GaPN mixed crystals. However, even if GaP and GaN were grown to have the same structure under appropriate growth conditions, the structure was unstable. GaP obtained by the above growth method has a low nitrogen concentration of about 2×10^{20} cm^{-3} at the maximum, and this has been used as a material for green light emitting diodes.

However, in the 1990s, as crystal growth technologies such as the Molecular Beam Epitaxy (MBE) method and the Metalorganic Vapor Phase Epitaxy (MOVPE) method progressed, nitrogen was added to the high extent of impurities [13,48]. These methods make it possible to grow GaPN alloys with a nitrogen concentration as high as 4-7%. Since it can be lattice-matched with Si at a nitrogen concentration of 2%, high-quality crystal growth is possible on a Si substrate.

2.5 Energy band structure of GaPN alloy semiconductor

With the realization of GaPN alloys with a high nitrogen concentration and the study of their physical properties, it has become clear that GaPN alloys have luminescence characteristics and electronic structures that general alloys do not have.

Figure 2.6 shows the photoluminescence spectrum of GaPN alloys.[36] It has been confirmed that in the GaPN alloy in the extremely low nitrogen concentration range (1) in the figure, sharp emission is observed from excitons bound to nitrogen atoms and nitrogen atom pairs. It has been reported that as the nitrogen concentration increases, the sharp luminescence formed by nitrogen shifts to broad luminescence (2), and when the concentration becomes higher, the luminescence shifts to the low energy side (3). The results of this emission spectrum indicate that the bandgap of the GaPN alloy decreases as the nitrogen concentration increases, suggesting that the GaPN alloy also has a very large bandgap bowing.

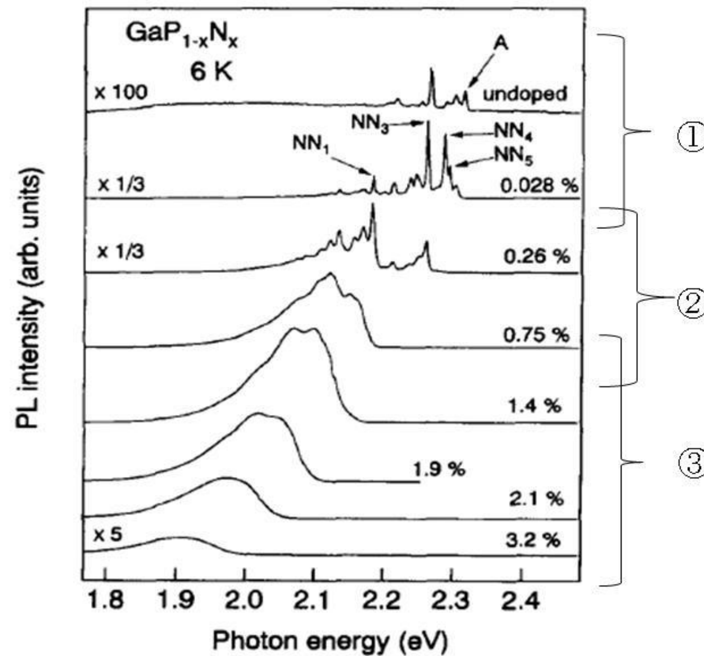

Figure 2.6 GaPN alloy photoluminescence spectrum.

In addition, the band structure of GaPN alloy was shown by first-principles calculation (Figure 2.7). In alloys with high nitrogen concentration, the wave functions of electron traps formed by nitrogen atoms overlap to form an IB. This suggests that GaPN alloys may be applicable as IBSCs. However, application to IBSCs requires knowledge of the carrier recombination process via the IB, CB, and NRR level.

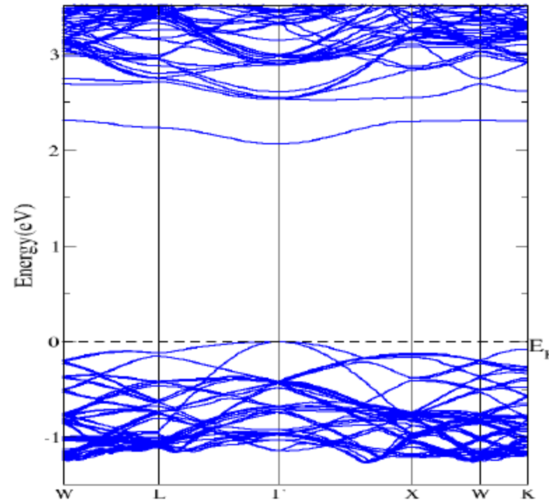

Figure 2.7 Band structure of GaPN alloy (nitrogen concentration 0.8%) shown by first-principles calculation.[49]

2.6 Shockley-Read-Hall (SRH) Recombination Theory

The important factor for solar cell devices is the carrier recombination mechanism. For realization of high efficiency solar cell, it is crucial to determine the recombination process. The defect inside the semiconductor materials can introduce energy level within the bandgap, they are known as trap level or NRR centers. The recombination of photo-generated electrons and holes at the NRR centers is the most crucial mechanism which influences the carrier lifetime, diffusion length, conversion efficiency and finally leading to device degradation. The electron and holes emission and capture mechanism had been explained and formulated firstly comprehensively by William Shockley and W. T. Read, Jr. [50] and by R. N. Hall [51] in 1952. These are known as the Shockley-Read-Hall (SRH) recombination statistics. The four possible transitions mechanism of an electron or hole between a NRR within the bandgap of a material and the conduction or the VB are indicated in Figure 2.8.

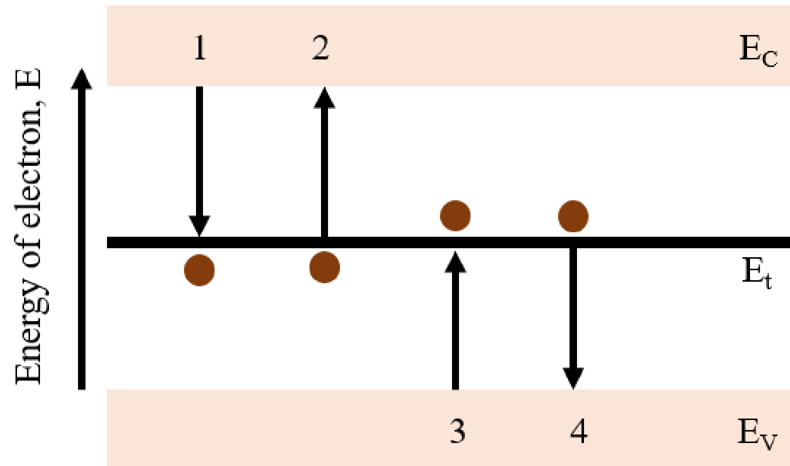

Figure 2.8 The basic processes involved in Shockley-Read-Hall recombination statistics.

There are four basic processes in Shockley-Read-Hall theory

1) Electron capture process: The capture of an electron from the CB to a neutral empty trap.

2) Electron emission process: This is the inverse process of electron capture. The electron back into the conduction by the emission from trap level.

3) Hole capture process: The capture of a hole from the VB by a trap. This can be depicted by a transition of a trapped electron from an unoccupied electron state to the VB.

4) Whole emission process: the emission of a hole from a neutral trap into the VB. It can be explained a capture of an electron from the VB.

Process 1: Electron capture rate

$$R_{cn} = C_n\left[N_t\left(1 - f_F(E_t)\right)\right]n,$$

where $f_F(E_t) = \frac{1}{1+\exp\left(\frac{E_t - E_f}{KT}\right)}$

Process 2: Election emission

$R_{en} = E_n[N_t f_F(E_t)]$

At thermal equilibrium

$R_{cn} = R_{en}$

$C_n[N_t(1 - f_F(E_t))]n = E_n[N_t f_F(E_t)]$

$$E_n = \frac{C_n(1 - f_F)n}{f_F(E_t)}$$

$$E_n = C_n\left(\frac{1}{f_F(E_t)} - 1\right)n$$

$E_n = C_n[1 + \exp\,(\frac{E_t - E_F}{KT})]N_c \exp\,(-\frac{E_c - E_F}{KT})$

$E_n = N_c \exp\,(-\frac{E_c - E_t}{KT})\, C_n$

$E_n = nC_n,$

where n $= N_c \exp\,(-\frac{E_c - E_t}{KT}) = n_i \exp\,(-\frac{E_t - E_i}{KT})$

The relation between emission constant and capture constant is valid at all conditions including when Fermi level is right located at trap energy, in which the trapping is the dominant process to provide the free electrons in the CB. The electron emission rate is increases exponentially as the trap energy level close to the CB.

Process 3: Hole emission rate

$R_{cp} = C_p[N_t f_F(E_t)]p$

Process 4: Hole emission rate

$R_{ep} = E_n[N_t(1 - f_F(E_t))],$

where $f_F(E_t) = \frac{1}{1+\exp\left(\frac{E_t - E_f}{KT}\right)}$

At thermal equilibrium

R_{cp}=R_{ep}

$C_p[N_t f_F(E_t)]p = E_n[N_t(1 - f_F(E_t))]$

$C_p p = E_P\left(\frac{1}{f_F(E_t)} - 1\right)$

$C_p N_v \exp\left(\frac{E_v - E_f}{KT}\right) = E_p[(1 + \exp(\frac{E_t - E_f}{KT}) - 1)]$

$= E_p \exp(\frac{E_t - E_f}{KT})$

$E_{p=} C_p N_v \exp\left(\frac{E_v - E_t}{KT}\right)$

$E_p = pC_p$

P $= N_v \exp\left(\frac{E_v - E_t}{KT}\right) = n_i \exp\left(\frac{E_i - E_f}{KT}\right)$

Capture constant: The electron capture constant comes from the electron with velocity v_{th}must come within a cross-sectional area of a trap to be captured and thus sweep out an effective trap volume per second. The same is for hole capture constant.

$C_n = v_{th}\sigma_{cn}$

$C_p = v_{th}\sigma_{cp}$

Emission constants: The electron emission rate from a trap is the product of electron capture rate and free carrier concentration when $E_f = E_r$

$E_n = n' C_n$

$n' = N_c \exp\left(-\frac{E_c - E_t}{KT}\right)$ and $p' = N_v \exp(\frac{E_v - E_t}{KT})$

Under non-equilibrium condition, the net electron capture rate at acceptor trap

$R_n = R_{cn} - R_{en}$

$R_n = C_n[N_t(1 - f_F(E_t))]n - E_n[N_t f_F(E_t)]$

$R_n = C_n N_t[n(1 - f_F(E_t)) - n f_F(E_t)]$,

where $n' = N_c \exp\left(-\frac{E_c - E_t}{KT}\right)$

The net hole capture rate at acceptor trap, $R_p = C_p N_t\left[p f_F(E_t) - p'\left(1 - f_F(E_t)\right)\right]$

$p' = N_v \exp\left(-\frac{E_v - E_t}{KT}\right)$

At steady sate $R_n = R_p$

$$f_F(E_t) = \frac{C_n n + C_p p'}{C_n(n + n') + C_p(p + P')}$$

$$n'p' = N_c \exp\left(-\frac{E_c - E_t}{KT}\right) N_v \exp\left(-\frac{E_t - E_v}{KT}\right) = N_c N_v \exp\left(-\frac{E_c - E_v}{KT}\right)$$

$$n'p' = n_i^2$$

$$R_n = R_p = \frac{C_n C_p N_t (np - n_i^2)}{C_n(n + n') + C_p(p + P')} \equiv R$$

For SRH-dominated recombination process, the recombination rate of excess carriers is,

$$R = \frac{\delta n}{\tau} = \frac{C_n C_p N_t\left(np - n_i^2\right)}{C_n(n + n') + C_p(p + P')}$$

2.7 Two-wavelength Excited Photoluminescence (TWEPL): A tool for non-radiative recombination centers characterization

The TWEPL is purely optical, non-contacting and non-destructive characterization technique for semiconductor material. Previously, Grimmeiss and Monemar characterized Cu-doped GaN by TWEPL in I 973 [52] who are the pioneer of this method. After that, the characterization of bulk GaP was done by Monemar and Samuelson by utilizing both the PL excitation (PLE) and the twofold excitation method. In early 1980's, Tajima investigated the deep defect levels in bulk GaAs by twofold excitation modulated PL technique [53]. He has successfully detected high concentration of NRR centers in bulk GaAs. In the early 1990, Kamata et al. characterized the NRR centers in GaAs/AIGaAs MQWs by TWEPL [54]. They had determined trap parameters of the NRR centers and

considered multi-level traps in GaAs/AlGaAs MQWs structures by the combination of time-resolved and TWEPL measurements. As a result of this successful quantitative determination of NRR parameters, TWEPL has been used for the characterization of GaAs/AlGaAs quantum wells [54], GaN/InGaN QWs [55], AlGaN QWs [56], GaPN [57], and $Ba_3Si_6O_{12}N_2:Eu^{2+}$phosphors [58].

It is indispensable to determine the spatial and energy distribution of NRR centers for classifying each defect state and determining its microscopic origin. It is possible to obtain energy distribution of NRR centers by using the BGE sources with deferent energies.

CHAPTER 3
EXPERIMENTAL DETAILS

3.1 Photoluminescence

Photoluminescence (PL) is a powerful optical method for probing the electronic structure of materials. It is a contactless, versatile, nondestructive method to obtain information on the internal optical processes and the optical quality of the material. The material is excited by light whose photon energy is higher than the bandgap of the material. The light is absorbed and imparts excess energy into the material in a process called photo-excitation. The electrons are excited from VB to the CB. The excited photo-carriers come to equilibrium condition via a radiative or NRR process. One of the ways to release excess energy from the material is through the emission of light. This is called luminescence. The luminescence intensity for the radiative recombination process is recorded as a function of wavelength to get a spectral plot. From the PL measurement, the information related to the bandgap of the material, defect levels, and the optical quality of the material can be obtained. The bandgap of the material is related to the peak wavelength of the PL spectra through the following equation:

$$E_g = \frac{hc}{\lambda},$$

Where, *h* is Planck constant and *c* is the speed of light.

3.2 Two-wavelength Excited Photoluminescence

In conventional PL, the sample is excited by the light source whose excitation energy is greater than the bandgap of the material($h\nu_{BGE} < E_g$), Hereafter, this excitation source is represented as AGE source. For the TWEPL, another BGE light whose photon energy is lower than the band-gap ($h\nu_{BGE} < E_g$) is superposed over AGE light of constant power in PL measurement. The PL intensity with and without BGE is recorded as $I_{AGE=BGE}$and as I_{AGE} respectively. The normalized PL intensity is defined byI_N =$I_{AGE=BGE}/\ I_{AGE}$. The deviation of the value of IN from unity indicates the presence of NRR centers in the materials. After irradiation of the BGE three cases can be happen:

(i) No change in PL intensity indicates that NRR center does not exist within the bandgap of the material whose energy corresponds to the energy of the BGE.

(ii) The increase in the PL intensity can be interpreted by one level model as shown in Fig. 3.1 (a). The BGE can excite the electrons from the VB to a NRR level or from a NRR level to the CB. As a consequence, an increase of either hole (Δp) or electron· (Δn) density in the VB and CB, respectively and the PL intensity increases due to its direct proportional relationship with the product of np.

(iii) The reduction of PL intensity can be explained by two levels model as shown in Fig. 3.1 (b). When the BGE energy corresponds to the energy difference between two coexisting NRR level, NRR level 1 and NRR level 2. Tue electrons in NRR level 1 are excited to NRR level 2, from where they recombine nonradiatively with holes in the VB. The diminution of the number of electrons in NRR level 1allows an increase of NRR process from the CB. The combination of both effects decreases the number of electron-hole pairs available for radiative recombination.

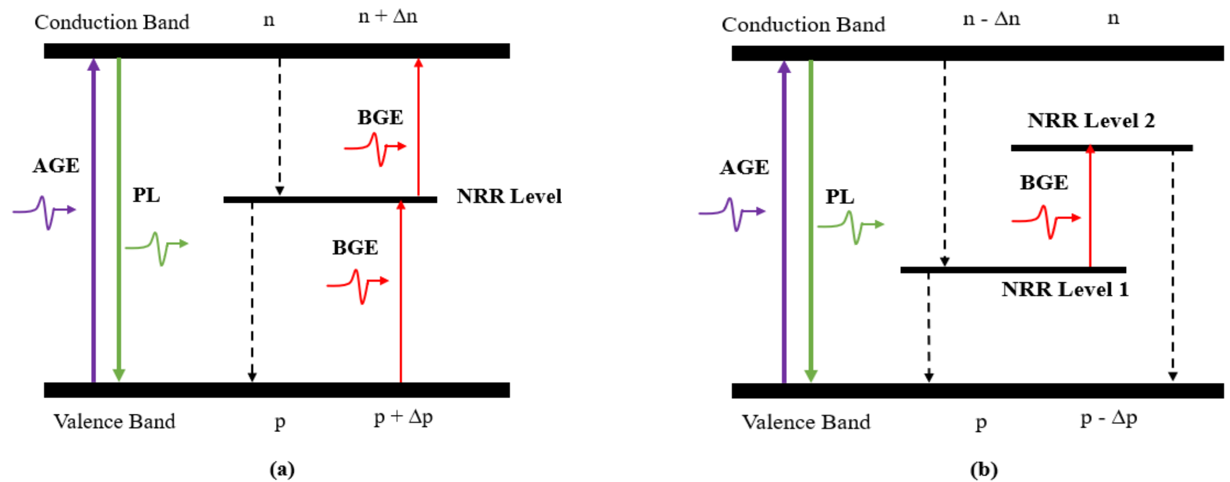

Figure 3.1 (a) One level model which explains the enhancement of the PL intensity, (b) Two levels model used for the illustration of the PL intensity quenching.

The typical experimental layout of the TWEPL is shown in Figure 3.2.

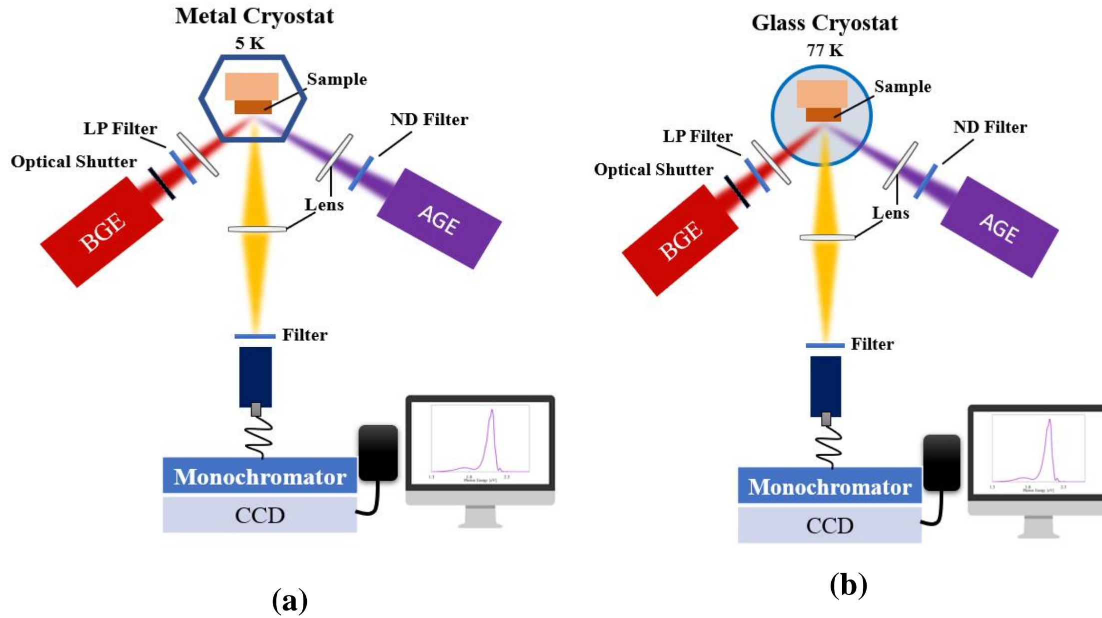

Figure 3.2 Experimental setup for TWEPL measurement (a) metal cryostat (b) glass cryostat.

For the characterization of GaPN alloy, the sample was mounted in a temperature-controlled metal cryostat. Then, it was excited by AGE light. The temperature of the metal cryostat was changed by a temperature controller and the change of PL spectra with temperature was recorded. At the stage of TWEPL, temperature is kept constant at 5 K and a BGE light with a photon energy $h\nu_B$ is switched on and off at the AGE spot of the sample. The output power of the AGE was kept constant and neutral density (ND) filters were used to change the excitation density. The PL signal from the sample was fed through a set of objective lenses to a QE Pro65000 (Ocean Optics) spectrometer with a CCD detector, which converts optical signals into photocurrent. A major difficulty of detecting NRR centers at $x = 0.105$ % sample was to discriminate the BGE effect from temperature quenching. There is a possibility of surface temperature rise due to irradiation of BGE on the sample. Therefore, we prepared a glass cryostat for the TWEPL measurement in which the sample was immersed in liquid nitrogen directly. In this case the temperature was

constant at 77 K. Two different light sources of AGE, a THG Nd: YAG laser with $h\nu_{A1}$= 3.49 eV (355 nm wavelength) and a semiconductor laser with $h\nu_{A2}$= 2.33 eV (532 nm), were used as CB excitation and IB excitation, respectively. We used the BGE light sources with energies 0.81 eV (1550 nm), 0.93 eV (1340 nm), 1.17 eV (1064 nm), 1.27 eV (980 nm), and 1.46 eV (850 nm). The sample was excited by one of AGE light, and the output power of AGE was kept constant. Neutral density (ND) filters were used for changing the excitation density and lens was used to focus the beam on the sample properly with an excellent spot size. The BGE light with a photon energy $h\nu_B$ was switched on and off at the same point of AGE spot of the sample. The signal of IB PL from the sample was fed to a fiber coupled QE65000 CCD spectrometer (Ocean Optics) for the detection which converts light signals into photocurrent and finally recorded by a computer. The long pass filters in front of detector were used to stop shorter wavelength component. We measure the PL intensities with and without the BGE, $I_{AGE+BGE}$ and I_{AGE}, respectively, and the normalized PL intensity is defined as

$$I_N = \frac{I_{AGE+BGE}}{I_{AGE}}$$

Its deviation from unity is interpreted as the presence of NRR centers activated by the BGE energy $h\nu_B$.

3.3 Sample Structure

Three samples of $GaP_{1-x}N_x$ with three different N concentration of $x = 0.105\%, 0.56\%$ and 0.75% were used in this research work. Figure 3.3 represents the structure of the $GaP_{1-x}N_x$ samples. The samples were grown by metalorganic chemical vapor deposition (MOCVD) technique. 300 nm-thick GaP buffer layer and 500 nm-thick $GaP_{1-x}N_x$ were grown in sequence on 400 µm-thick doped GaP substrate with an orientation of (100). $GaP_{1-x}N_x$ (0.105%) and $GaP_{1-x}N_x$ (0.75%) samples were grown on sulfur doped GaP substrates. $GaP_{1-x}N_x$ (0.56%) sample was grown on undoped GaP substrate. Trimethylgallium, phosphine, and dimethylhydrazine were used as Ga, P, and N sources, respectively.

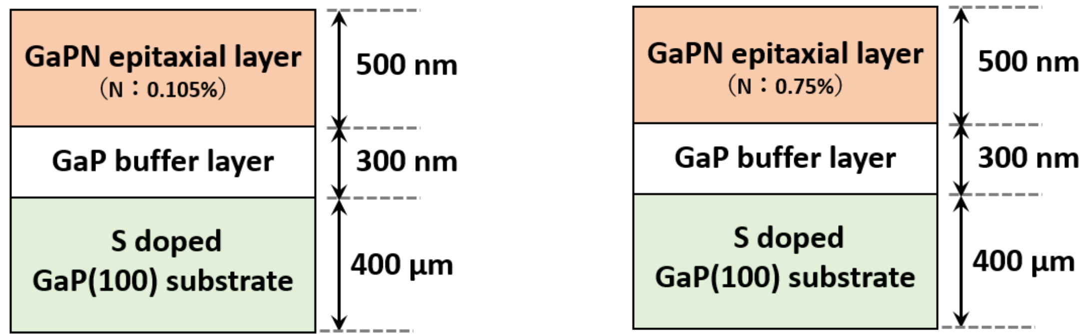

(a)

(b)

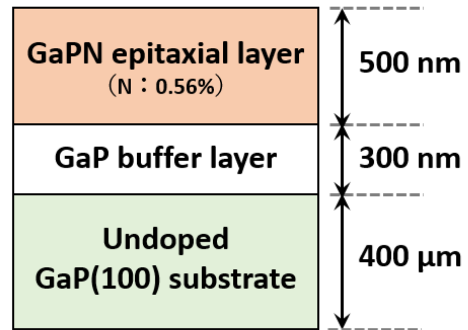

(c)

Figure 3.3 Schematic diagram of $GaP_{1-x}N_x$ sample structures.

CHAPTER 4

CHARACTERIZATION OF NONRADIATIVE RECOMBINATION CENTERS IN GaPN (0.105%)

4.1 Introduction

The detection and characterization of NRR centers of $GaP_{1-x}N_x$ (x=0.105%) samples was studied by a purely optical and non-destructive technique of TWEPL method. With the irradiation of an intermittent BGE light and investigating its impact on the IB photoluminescence under two kinds of AGE light (CB or IB excitation), we have interpreted a schematic energy diagram of NRR processes among CB, IB and VB.[59,60] By combining experimental data of TRPL, solving the rate equations based on the postulated energy diagram and fitting the results with experimental data of TWEPL, the relative contribution of NRR parameters is evaluated.

4.2 Results and Discussion

4.2.1 Temperature Dependence

Figure 4.1 (a) shows the temperature-dependent PL spectra of $GaP_{1-x}N_x$ (x= 0.105%) between 5 K and 80 K. The PL spectrum of x=0.105% sample at 5 K consists of NN_1 (2.18 eV), NN_3 (2.26 eV), NN_4 (2.28 eV) and their phonon replicas.[20] The change of their spectral shape normalized at $h\nu$=2.18 eV is shown in Figure 4.1 (b). Figure 4.1 (c) shows the intensity of 5 dominant peaks in Figure 4.1 (a) as a function of temperature. It is observed that a strong quenching of each peak, especially those with photon energies higher than 2.2 eV, takes place with increasing temperature from 5 K to 80 K. The peak energy of PL spectra shifts to lower energies with increasing temperature as shown in Figure 4.1 (b). As electronic energy distribution becomes wider with higher thermal energy, electronic redistribution from higher localized energy level to lower delocalized state becomes dominant. That is the reason why the PL spectra show lower energy shift. We consider that the N concentration x=0.105% is important because its PL spectrum as a function of temperature exhibits a change of dominant character from localized electronic level to spatially-overlapped IB as well as band-gap shrinkage.

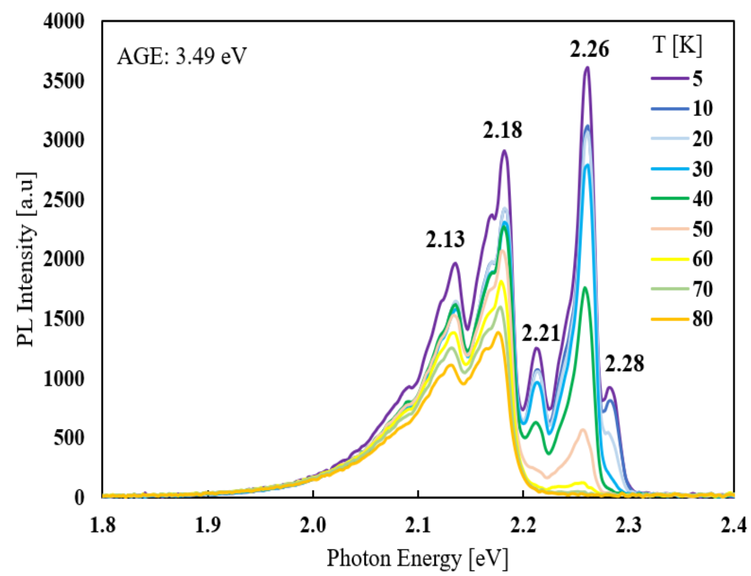

(a)

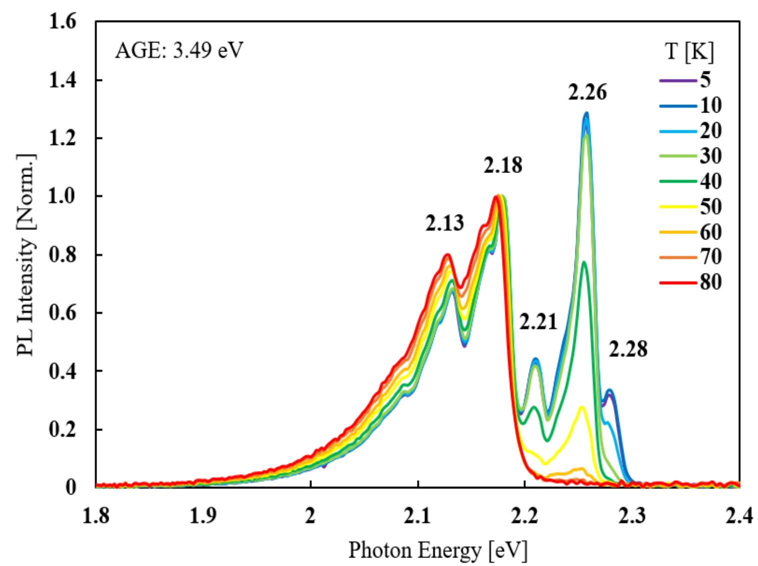

(b)

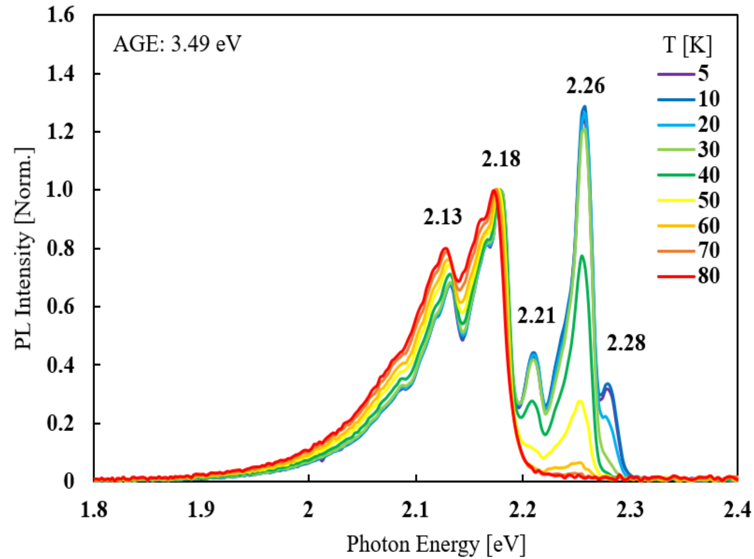

(c)

Figure 4.1 (a) Temperature-dependent PL spectra (b) Normalized PL spectra with increasing temperature (c) The intensity of 5 dominant peaks in Figure (a) as a function of temperature.

4.2.2 PL Intensity

The PL intensity was measured in liquid N_2 without superposing the BGE light. Figure 4.2 (a) and (b) show the AGE intensity dependence of PL spectra for CB excitation (3.49 eV) and IB excitation (2.33 eV), respectively. Two dominant peaks are found at 2.13 and 2.18 eV at 77 K and the PL intensity increased with increasing the AGE power density. The integrated PL intensity was calculated from each spectrum as a function of AGE photon number density for both CB and IB excitation, as shown in Figure 4.2 (c). The integrated PL intensity increases monotonously with increasing AGE photon number density for both CB and IB excitation without showing any saturating tendency. The integrated PL intensity for the IB excitation is higher than that of the CB at the same AGE photon number density, thus showing a higher emission efficiency of the IB.

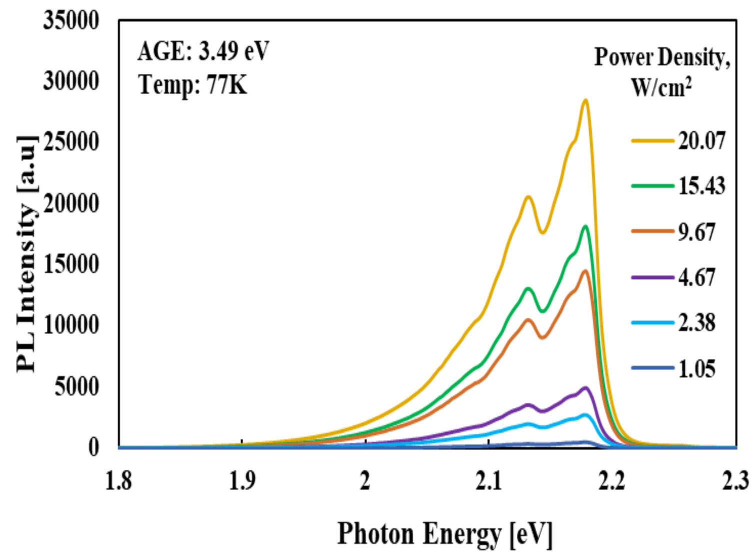

(a)

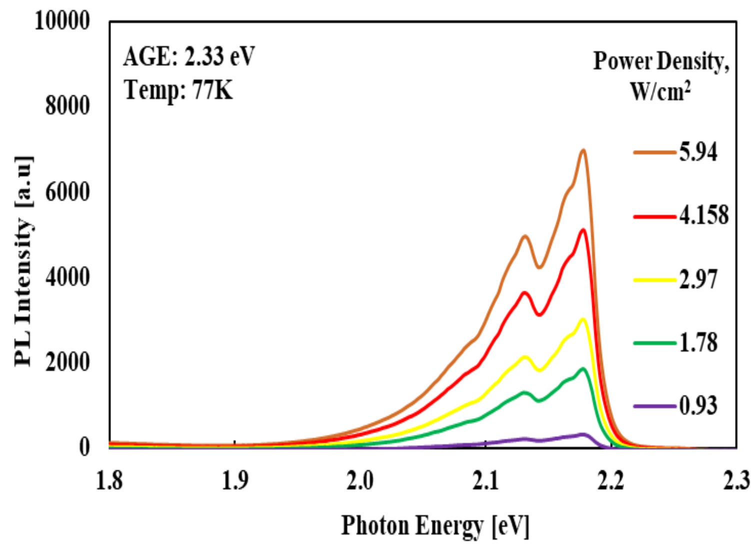

(b)

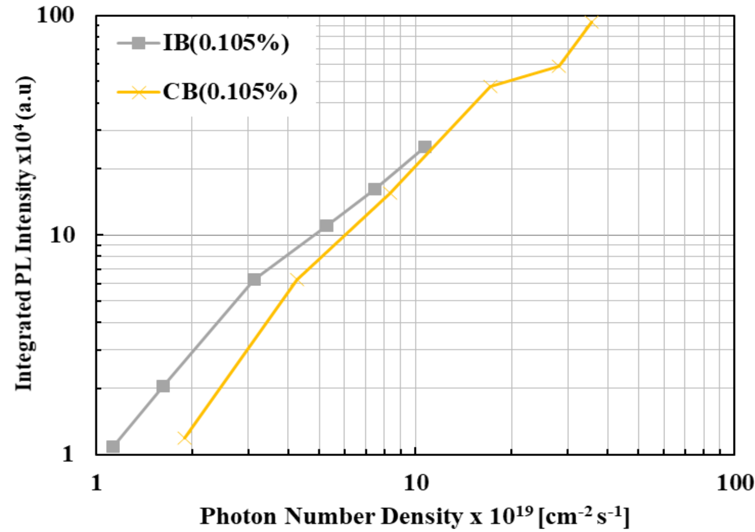

(c)

Figure 4.2 AGE power density dependent PL intensity for (a) CB excitation and (b) IB excitation. (c) Integrated PL intensity for IB and CB excitation.

4.2.3 Characterization of NRR centers

In this study, the detection and characterization of NRR centers were done by using TWEPL method. The PL intensity changes when BGE light is superposed over AGE light. It is difficult to exclude a possibility of surface temperature rise when BGE is superposed over AGE at room temperature. A slight temperature rise produces thermal depopulation of N-related states starting from shallower-energy (i.e., higher photon-energy) side. That means temperature rise activates transition to NRR centers and it quenches PL intensity. For this reason, we eliminated the temperature effect by immersing the sample into liquid N_2.

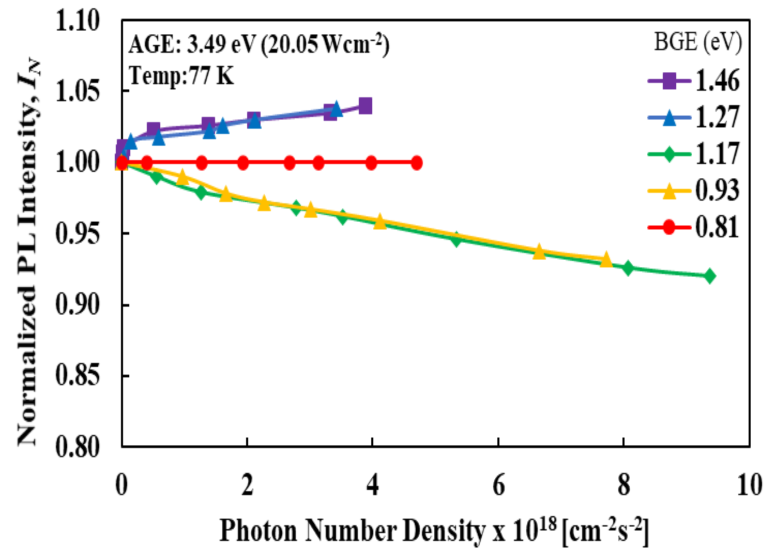

(a)

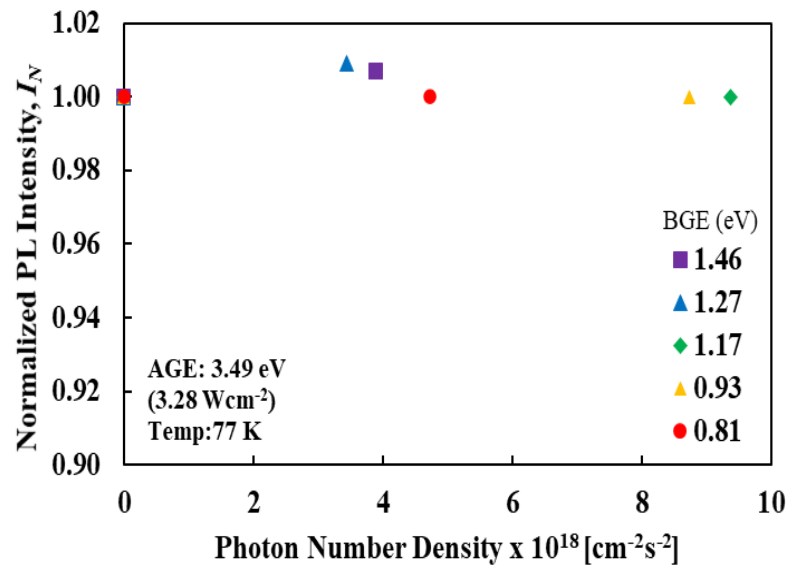

(b)

Figure 4.3 I_N values as a function of BGE photon number density for CB excitation with AGE (a) 20.04 Wcm^{-2} and (b) 3.28 Wcm^{-2}.

For the characterization of NRR centers, the normalized PL intensity, I_N was measured as a function of BGE photon number density for five BGE energies as 0.81, 0.93, 1.17, 1.27, and 1.46 eV, respectively, as shown in Figure 4.3 (a) and (b) for CB excitation. The AGE power density was fixed at 20.05 Wcm^{-2} for Figure 4.3 (a). When BGE (1.27 and 1.46 eV) is superposed over AGE, the value of I_N increases from unity. The maximum

value of $I_N = 1.04$ is observed for 1.46 eV BGE with a photon number density of 3.8×10^{18} cm^{-2}s^{-1}. For 0.93 and 1.17 eV BGE, the value of I_N decreases from unity. It implies the presence of a pair of NRR centers in the sample whose energy difference corresponds to that of the BGE energies. The most dominant quenching of the value of $I_N = 0.92$ is observed for 1.17 eV BGE for a photon number density of 9.37×10^{18} cm^{-2}s^{-1}. There is no change of I_N for 0.81 eV BGE. The AGE power density was lowered down to 3.28 Wcm^{-2} for Figure 4.3 (b). In this case, the value of I_N increased also for 1.27 and 1.46 eV BGE, but there is no change of I_N for other BGE energies.

Figure 4.4 (a) and (b) show the normalized PL intensity for IB excitation. The change of I_N value shows the similar tendency as that of CB excitation. The deviation of I_N from unity indicates the presence of NRR centers for both cases. BGE energy of 1.27 and 1.46 eV show almost the same increase of I_N value both for CB and IB excitation. It implies that the densities of NRR centers corresponding to these two BGE are in a similar order of magnitude. By the same way, it can be explained that the densities of NRR centers corresponding to 0.93 and 1.17 eV are almost similar.

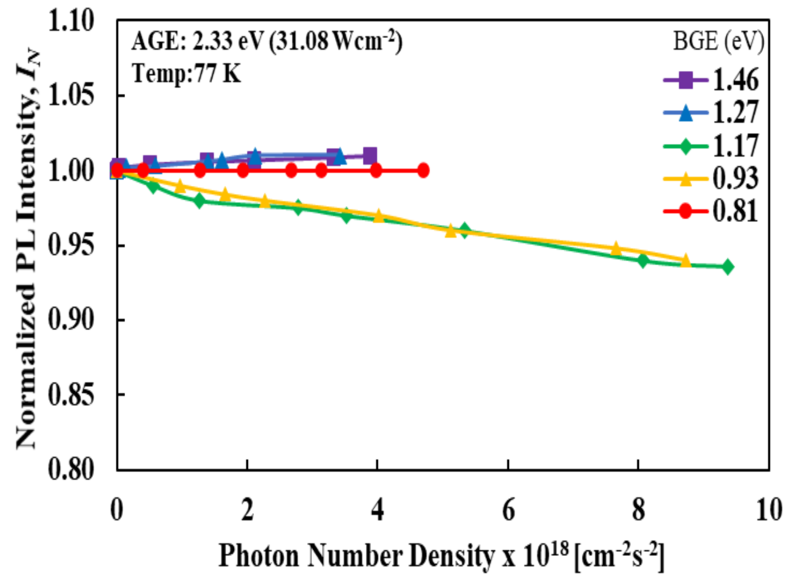

(a)

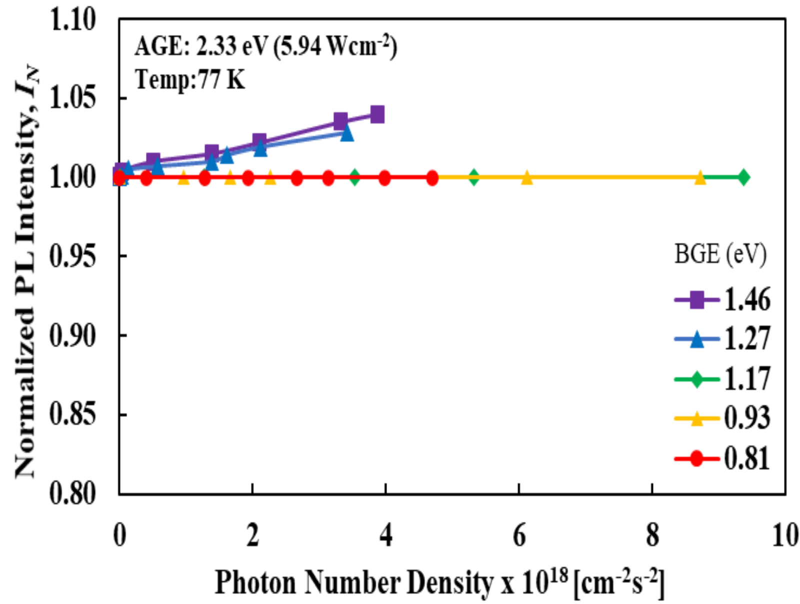

(b)

Figure 4.4 I_N values as a function of BGE photon number density for IB excitation with AGE (a) 31.08 Wcm^{-2} and (b) 5.94 Wcm^{-2}.

Figure 4.5 shows the schematic energy diagram of NRR processes among CB, IB and VB according to the I_N values for high excitation energy of AGE. According to the previous studies devoted to DLTS characterization of similar material, the observed NRR level is close to the middle of the bandgap.[61] With AGE energy density of 20.05 Wcm^{-2} for CB excitation and 31.08 Wcm^{-2} for IB excitation, the 0.81 eV BGE shows no effect. Whereas BGE of 0.93 and 1.17 eV show the quenching of PL intensity which follow two-level model. These results imply that there is an energy-distributed NRR level near 1.10 eV (NRR1) which acts as two-level model with extended state of CB (2.27 eV) for 1.17 eV BGE, and with NRR3 (2.03 eV) for 0.93 eV BGE. For 1.27 and 1.46 eV BGE, the NRR1 acts as one-level model, which is the reason for the increase of PL intensity.

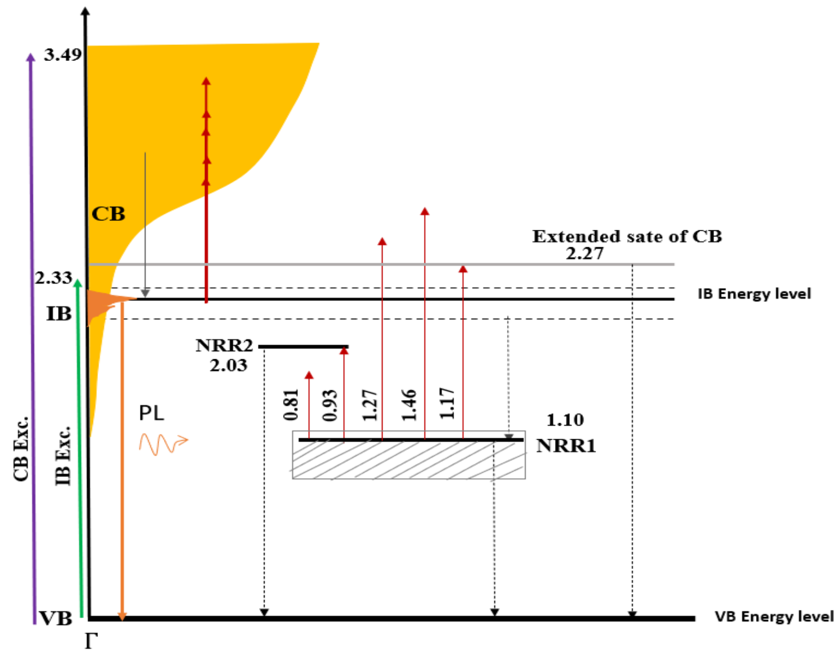

Figure 4.5 Schematic energy diagram of NRR processes in $GaP_{1-x}N_x$ (x=0.105%) alloy for high excitation energy of AGE. The spectrum of IB-PL (colored by orange) indicates the position of the IB. Purple line shows the electron excitation from VB to CB, Green line shows the electron excitation from VB to IB, and red line shows BGE excites electrons from the IB states to CB and from NRR level to CB and other NRR level. The dashed line indicates the nonradiative recombination of electrons.

For AGE with low energy density, the I_N values show that there is no effect for 0.81, 0.93, and 1.17 eV BGE. Since the Fermi level of the NRR1 shifts to lower energy side at lower AGE density, the initial-state of the BGE process shifts to lower energy level. That is why the energy difference between NRR1 and NRR2 does not match for these three BGE energies which results no change of the PL intensity (Figure 4.6). We consider that the Fermi-energy of NRR1 is lowered down to 0.90 eV which acts as one-level model for 1.27 and 1.46 eV BGE since electrons at the level are excited to the IB for these two BGE energies.

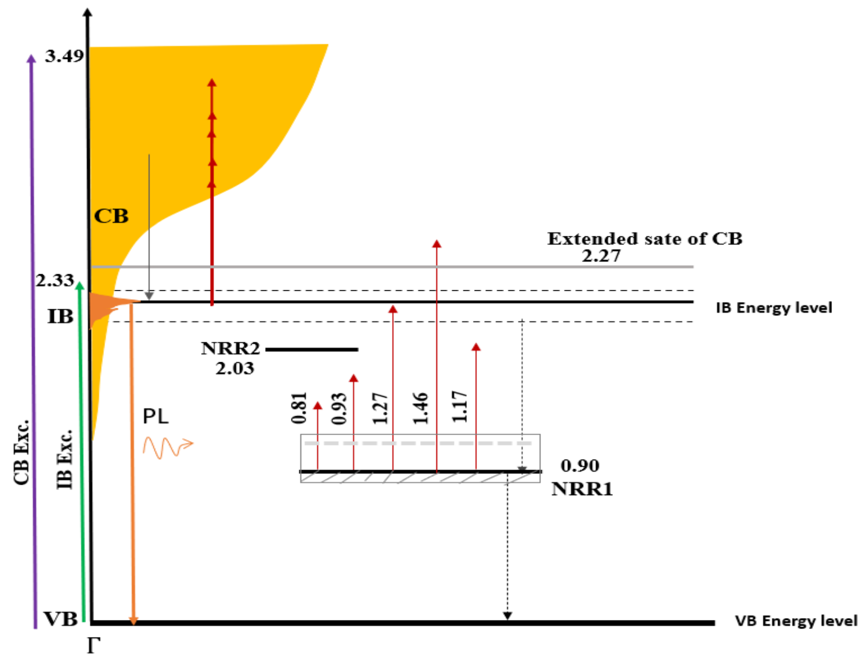

Figure 4.6 Schematic energy diagram of NRR processes in $GaP_{1-x}N_x$ (x=0.105%) alloy for low excitation energy of AGE. The spectrum of IB-PL (colored by orange) indicates the position of the IB. Purple line shows the electron excitation from VB to CB, Green line shows the electron excitation from VB to IB, and red line shows BGE excites electrons from the IB states to CB and from NRR level to IB and CB. The dashed line indicates the nonradiative recombination of electrons.

The basis of this interpretation is originated from the BGE effect which is same with previous interpretation.[62, 63] Since the band-gap energy as well as the center position of the IB depend on N concentration, the position of the NRR centers also shifts according to the band-gap energy. Here the lower N concentration sample has the lower density of states in the mid-gap level. Hence the shift of Fermi-energy in the mid-gap level depending on the AGE photon number density plays an important role in this interpretation which is an important concept for the N concentration of 0.105%.

4.2.4 Time-resolved PL Measurement and Determination of Trap Parameters by Rate Equation Analysis

In order to consolidate our qualitative interpretations according to a postulated energy diagram shown in Figure 4.6 and measured lifetime, a quantitative simulation of the

TWEPL results was carried out for the most dominant PL increase occurred by the 1.46 eV BGE for the low power density of IB excitation. The increase of PL intensity was not so significant at low power density of CB excitation. The rate equations for one-level model for IB excitation can be written as,[59,64-66]

$$\frac{dn}{dt} = G_1 - Bnp - nC_{n1}N_{t1}(1 - f_{t1}) + G_2N_{t1}f_{t1} = 0; \quad (4.1)$$

$$\frac{dp}{dt} = G_1 - Bnp - pC_{p1}N_{t1}f_{t1} = 0; \quad (4.2)$$

$$\frac{df_{t1}}{dt} = nC_{n1}(1 - f_{t1}) - pC_{p1}f_{t1} + G_2f_{t1} = 0; \quad (4.3)$$

$$n_0 + p = n + N_{t1}f_{t1} = 0; \quad (4.4)$$

where the radiative recombination coefficient B is measured as 4.33×10^{-11} cm^3 s^{-1} for $GaP_{1-x}N_x$ $(x = 0.105\%)$ sample. The generation rate of the AGE (G_1) is calculated experimentally by using following expression,[67, 68]

$$G_1 = \frac{P_{laser}(1-R)\alpha}{A_{spot}h\nu}, \quad (4.5)$$

where P_{laser} is the excitation power, R (18%) is the Fresnel reflection at the sample surface, A_{spot} is the laser spot size on the sample surface, $h\nu$ is the photon energy of the excitation leaser, and α is the absorption coefficient of the $GaP_{1-x}N_x$ $(x = 0.105\%)$ sample. It is impossible to evaluate the BGE coefficient (G_2) from the absorption coefficient measurement since no fundamental absorption occurs for these BGE sources.

To better understand the recombination mechanism in $GaP_{1-x}N_x$ $(x = 0.105\%)$, Time-resolve Photoluminescence (TRPL) measurements are performed. Figure 4.7 shows the PL decay profile of $GaP_{1-x}N_x$ $(x = 0.105\%)$ at 77 K for CB excitation (470 nm, 2.64 eV). The PL decay curves are fitted by using multiexponential function (4.6),[40,69-70]

$$I(t) = \sum_{i=1}^{n} A_i \exp\left(-\frac{t}{\tau_i}\right) \quad (4.6)$$

where, A_i and τ_i represent the amplitude and decay time of each exponential component. In our case, three exponential components (4.7) were needed to well fit the experimental data. In Figure 4.7, the orrange line shows the fitting curve for CB excitaion. The exciton lifetime is determined by radiative recombination, nonradiative recombination and relaxation to other radiative levels. The fast decay observed in the PL decay profile (Figure 4.7) is considered to correspond to the case where excitons exist near nonradiative centers. τ_1 is mainly determined by the nonradiative lifetime because the nonradiative recombination process is much faster than the other two processes. τ_2 is dominated by the radiative recombination and relaxation to other radiative levels. τ_3 is related to longer process with lower importance here. The calculated decay times are shown in Table 4.1.

$$I = A_1 e^{-\frac{t}{\tau_1}} + A_2 e^{-\frac{t}{\tau_2}} + A_3 e^{-\frac{t}{\tau_3}} \tag{4.7}$$

Table 4.1. PL decay time of $GaP_{1-x}N_x$ (x=0.105%) for CB excitasion.

Excitaion (nm)	τ_1 (ns)	τ_2 (ns)	τ_3 (ns)
470	3.27	17.71	576.49

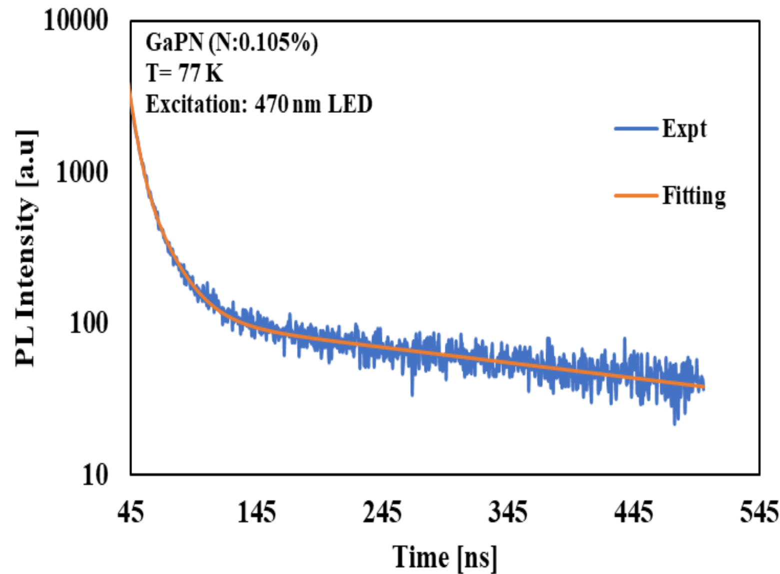

Figure 4.7 PL decay profile of $GaP_{1-x}N_x$ ($x = 0.105\%$) with fitting curve under CB excitation.

With optical excitation, a part of photogenerated holes in VB is captured by the NRR center. As excitation power increases, the NRR centers are gradually filled up with holes, so that f_{t1} approaches zero from its equilibrium value one. The decrease of f_{t1} weakens the further transition of holes from the VB and, hence, decreases the NRR rate. At thermal equilibrium condition (G=0), the relation $n_0 > N_{t1}$ yields f_{t1}=1. Hence, at low excitation limit of AGE excitation f_{t1}=1, which gives the expression of τ_1 from equation (4.2),[64]

$$\tau_1 = \frac{1}{B(n_0 - N_{t1}) + C_{p1}N_{t1}} \approx \frac{1}{C_{p1}N_{t1}} \tag{4.8}$$

Thus, a relationship between C_{p1} and N_{t1} is obtained from TRPL measurement. By using a set of C_{p1} and N_{t1} values, which satisfy equation (4.8), the calculated value of τ_1 is 3.24 ns which is very near to the experimental value of 3.27 ns. The calculated values of trap parameters are tabulated in Table 4.2.

Table 4.2. Values of C_{p1} and N_{t1} for $GaP_{1-x}N_x$(x=0.105%) determined by TRPL measurement.

B ($cm^3 s^{-1}$)	n_0 (cm^{-3})	C_{p1} ($cm^3 s^{-1}$)	N_{t1} (cm^{-3})
4.33×10^{-11}	5.0×10^{15}	2.8×10^{-6}	1.1×10^{14}

The system of rate equations can be solved numerically and the dependencies of n, p, and f_{t1} on G_2 can be found for the constant parameters of G_1, B, and n_0 and NRR1 dependent parameters C_{n1}, C_{p1}, and N_{t1}. The values of C_{p1} and N_{t1} of $GaP_{1-x}N_x$ ($x = 0.105\%$) are already determined by TRPL measurement. By systematically solving and fitting the results with experimental data, all the NRR parameters are obtained as shown in Table 4.3.

Table 4.3. Trap parameters of the dominant NRR1 center for IB excitation.

Excitaion (nm)	G_1 ($cm^3 s^{-1}$)	B ($cm^3 s^{-1}$)	n_0 (cm^{-3})	C_{n1} ($cm^3 s^{-1}$)	C_{p1} ($cm^3 s^{-1}$)	N_{t1} (cm^{-3})
532	3.9×10^{23}	4.33×10^{-11}	5.0×10^{15}	5.1×10^{-9}	2.8×10^{-6}	1.1×10^{14}

Figure 4.8 (a) shows the variation of I_N values as a function of the electron-hole generation rate (G_2) of the 1.46 eV BGE at 77 K under IB excitation with a fixed generation rate of 3.9×10^{23} cm^{-3} s^{-1}. The solid square (orange) and broken (orange) line represent the experimental and simulated data of I_N values, respectively. The simulated I_N values exhibit a reasonable agreement with the experimental data. The variation of normalized PL intensity as a function of the electron-hole generation of IB excitation (G_1) at 77 K is calculated by setting $G_2 = 1 \times 10^{11}$ cm^3 s^{-1} for 1.46 eV BGE and keeping all the parameters same as previous calculations.

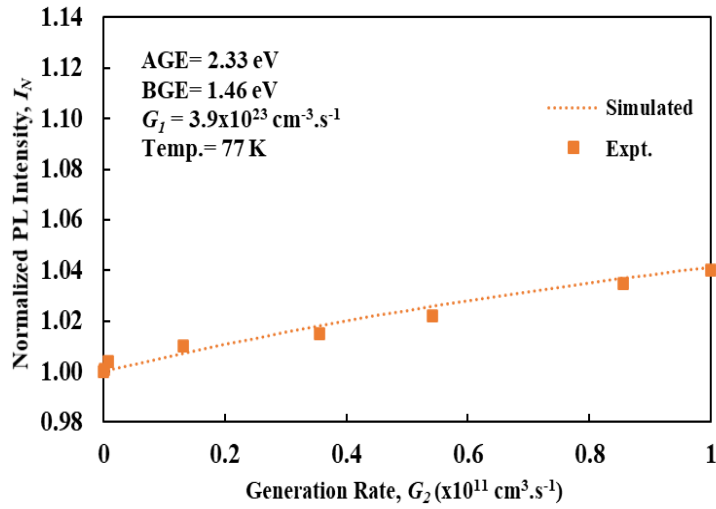

(a)

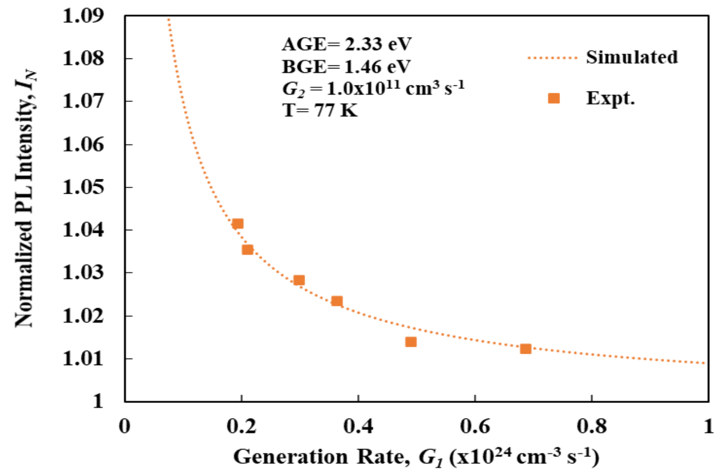

(b)

Figure 4.8 (a) Variation of I_N values as a function of G_2 and (b) Variation of I_N values as a function of G_1 at 77 K for 1.46 eV BGE for IB excitation.

Figure 4.8 (b) shows the depicted results along with experimental results. Here, a set of parameters give the behavioral insight into below-gap states acting as NRR1 center in $GaP_{1-x}N_x$ ($x = 0.105\%$), and there is a reasonable fitting with the experimental data. Although this set of parameters (Table 4.3) shows a reasonable fit with AGE and BGE photon number density dependence under IB excitation, the possibility of another set of parameters should not be ruled out. Actual excitation and recombination processes take place in parallel, and the situation becomes more complex. However, it is clear that the one-level model is valid as the fundamental NRR process for interpreting our experimental results. It gives us a way of detecting and characterizing NRR centers.

4.3 Conclusion

The NRR centers in $GaP_{1-x}N_x$ ($x = 0.105\%$) have been studied by using TWEPL method. The PL spectra of IB showed a shift toward lower energy-side with increasing temperature. The temperature effect due to BGE irradiation on sample was eliminated by immersing it in liquid N_2 and the TWEPL method revealed the presence of NRR centers in $GaP_{1-x}N_x$ ($x = 0.105\%$). Depending on the excitation energies of BGE, different contribution of one-level model and two-level model took place for CB and IB excitation. The effect of BGE energies depends also on the AGE excitation power density through a shift of Fermi energy in the forbidden energy gap. These results are successfully interpreted by a distribution of NRR centers and NRR process among CB, IB and VB by using TWEPL method. By combining the result of TRPL with that of TWEPL in a simulation of rate equations, the NRR parameters were evaluated. The results of fitting are consistent with experimental data and justify the consideration of recombination model.

CHAPTER 5

CHARACTERIZATION OF NONRADIATIVE RECOMBINATION CENTERS IN GaPN (0.56%)

5.1 Introduction

Combination of experimental intensity change as a function of the BGE density with the rate equation analysis of trap filling effect based on the SRH statistics enabled us to open a way of determining NRR parameters quantitatively as the scheme of TWEPL. With continuation of our study of detecting NRR centers in $GaP_{1-x}N_x$ with N concentration $x = 0.105\%$, here we focus on detection and characterization of NRR centers at $x = 0.56\%$. On lower N concentration region, the PL spectrum of GaPN originates from isoelectronic trap and NN_i pairs and it merges to that of IB with increasing N concentration. Since the carrier recombination process via IB is different due to a slight change in N concentration, it is demonstrated that the amount of N has a large effect on the physical properties. Characterization of NRR levels in higher concentration sample is essential to predict the optimum condition of GaPN alloy for advancing the application of IBSCs.

5.2 Results and Discussion

5.2.1 PL Intensity

PL spectra were measured at 77 K (in liquid N_2) with a variation of AGE excitation power density for both IB and CB excitations as shown in Figure 5.1 (a) and (b). The dominant peak is at 2.12 eV in both cases of the IB and the CB excitations without any change in spectral shape. Figure 5.1 (c) shows integrated PL intensity calculated as a function of AGE photon number density for both the IB and the CB excitations. The integrated PL intensity under the IB and the CB excitations increases almost linearly with increasing AGE photon number density. In spite of large difference in absorption coefficient, the integrated PL intensity for the IB excitation is higher than that of the CB at the same AGE photon number density, thus showing a higher emission efficiency of the IB.

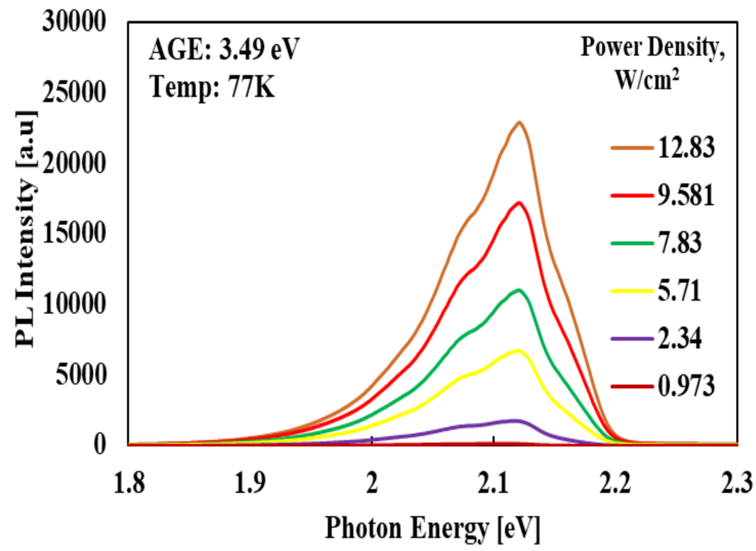

(a)

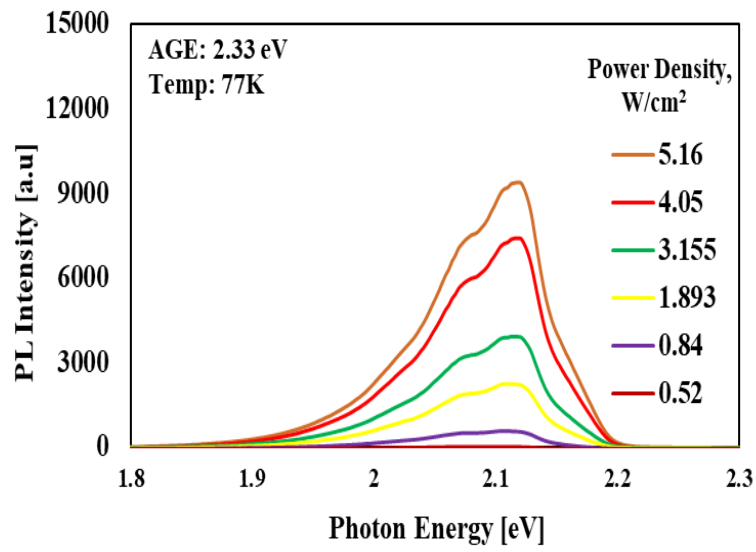

(b)

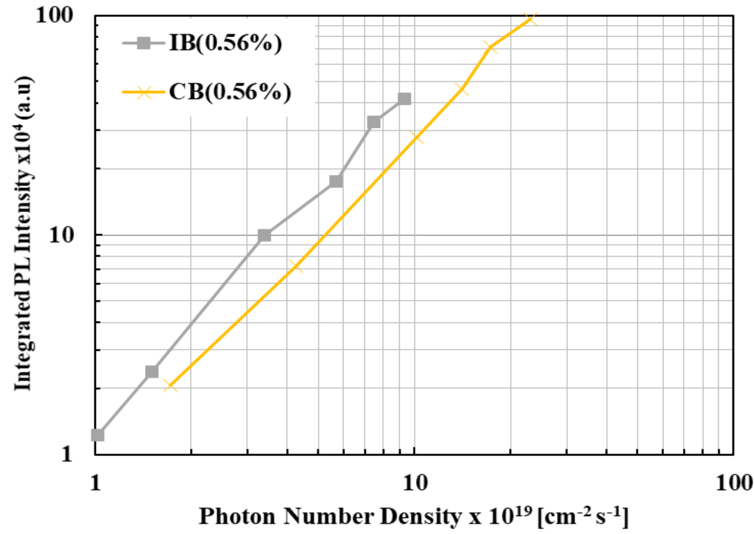

(c)

Figure 5.1 AGE power density dependent PL intensity for a) CB excitation and b) IB excitation. c) Integrated PL intensity for IB and CB excitation.

5.2.2 BGE Dependence of the PL Intensity

In order to know the distribution of NRR centers in $GaP_{1-x}N_x$ ($x = 0.56\%$) sample, the normalized PL intensity (I_N) was measured as a function of the BGE photon number density for five BGE energies as 0.81, 0.93, 1.17, 1.27, and 1.46 eV, respectively. The variation of I_N values as a function of BGE photon number density for the IB excitation is shown in Figure 5.2 (a). Here, the AGE power density was fixed at 5.16 W cm^{-2}. When BGE is superposed over the AGE, the values of I_N increased from unity for all BGE energies. It is observed from Figure 5.2 (a) that the amount of PL increase becomes pronounced with increasing BGE photon number density and gradually tends to be saturated. The most dominant increase of I_N value 1.11 occurred by the 1.46 eV BGE energy with a photon number density of 6.3×10^{18} cm^{-2} s^{-1}. We need to distinguish two BGE processes in our GaPN: one is the BGE process from the IB to the CB, while the other is that from NRR centers to the IB. It can be accomplished by considering the BGE energy dependence. In the former process from the IB to the CB, any final states of BGE from the IB are allowed as they are allocated inside CB. Thus, the former BGE process from the IB

to CB shows no specific BGE energy dependence, but a common part among different BGE energies. On the contrary, a clear BGE energy dependence shown in Figure 5.2 (a) implies that the dominant BGE process is not from the IB to CB, but the process of NRR levels.

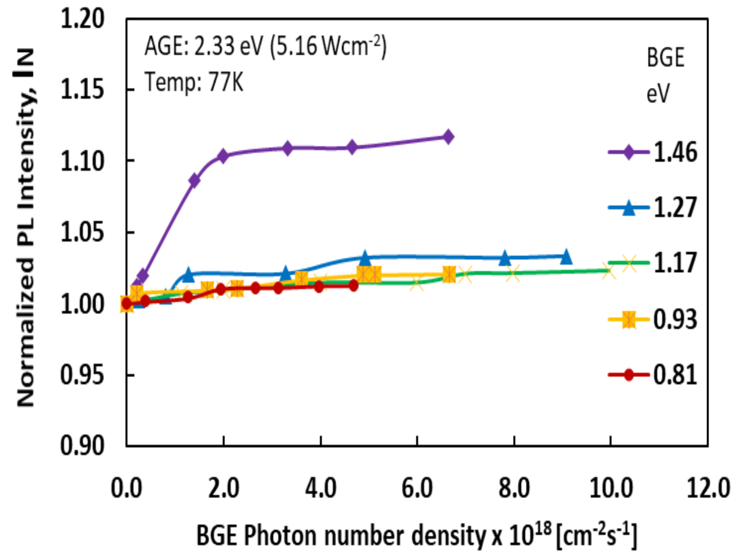

(a)

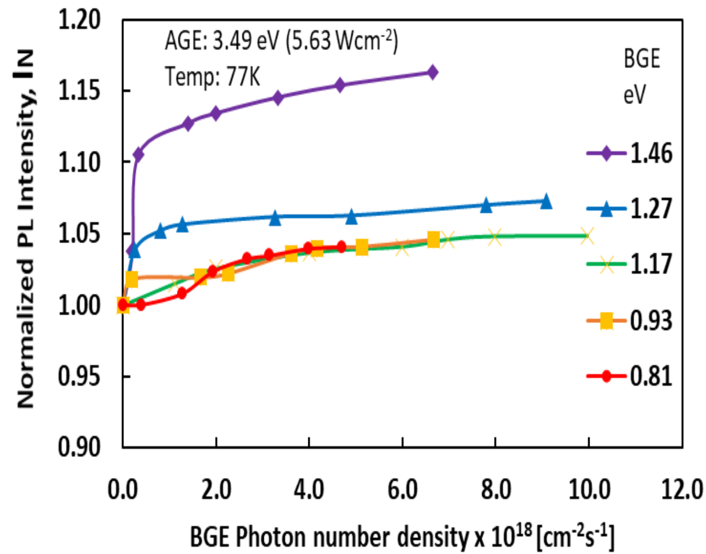

(b)

Figure 5.2 Variation of I_N values as a function of BGE photon number density for (a) IB and (b) CB excitation.

Figure 5.2 (b) shows the variation of I_N values as a function of BGE photon number density for the CB excitation. The AGE power density was fixed at 6.41 Wcm^{-2} in this case. With the addition of BGE light on the AGE, the values of I_N increased from unity for all BGE energies as same as the IB excitation. It is observed from Figure 5.2 (b) that the normalized PL intensity increases with increasing BGE photon number density and then it shows a saturating tendency at higher photon number density. The most dominant increase of the I_N value 1.16 occurred by the 1.46 eV BGE energy with a photon number density of 6.3×10^{18} cm^{-2} s^{-1}. The increase of I_N values from unity suggests the BGE process again from IB to CB and/or from NRR centers to the IB or CB. A distinct energy dependence shown in Figure 5.2 (b) implies that the dominant BGE process is the latter one. Therefore, our experimental results shown in Figure 5.2 (a) and (b) are effective for characterizing NRR centers in $GaP_{1-x}N_x$ ($x = 0.56\%$).

5.2.3 Characterizations of NRR centers

Figure 5.3 shows a schematic energy diagram of optical excitation and carrier recombination processes which explains the PL intensity increase due to the irradiation of the BGE. In IB and CB excitation, it is observed that the most dominant increased in PL intensity occurred for 1.46 eV BGE according to Figure 5.2 (a) and (b). Considering I_N values for all five BGE energies, a NRR level is allocated at 0.66 eV above VB. When the BGE light irradiates on the $GaP_{1-x}N_x$ ($x = 0.56\%$) sample, electrons are excited from NRR to IB as well as excited from IB to CB. The maximum electron excitation from NRR to IB takes place for 1.46 eV BGE since the energy difference matches properly for that BGE. It is observed from PL intensity measurement that the PL intensity starts from 1.9 eV. For 1.27 eV BGE, electrons can excite from NRR1 to the IB as well as from the IB to the CB and I_N value increased for 1.27 eV BGE. It is considered that the NRR level is at 0.66 eV above VB. Actually, the NRR level is a discrete energy level. So, there is a possibility to excite some electrons from discrete NRR level to IB also for 0.93 and 0.81 eV BGE which is responsible for small increase of I_N value.

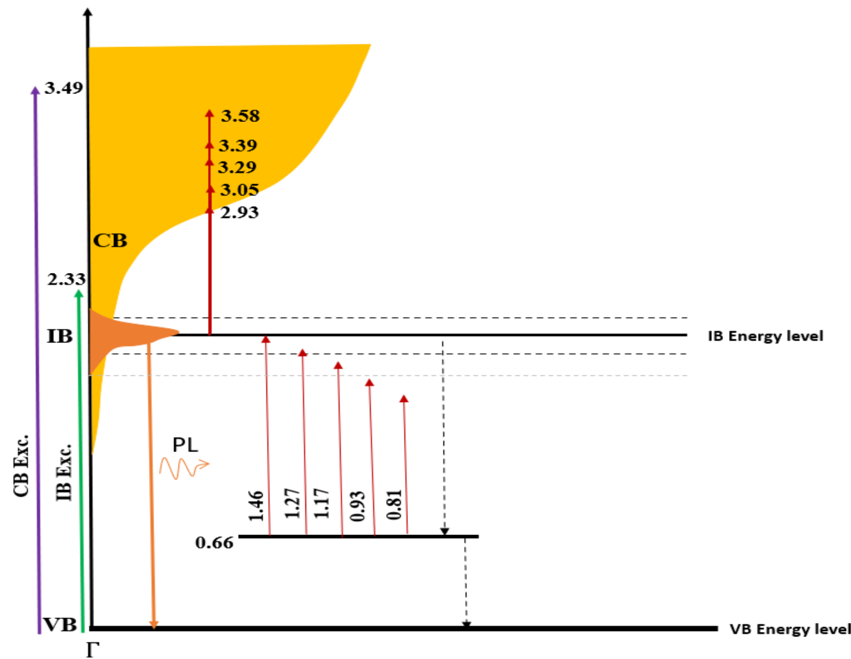

Figure 5.3 Schematic energy diagram of NRR processes in $GaP_{1-x}N_x$ (x=0.56%) alloy. The spectrum of IB-PL (colored by orange) indicates the position of the IB. Purple line shows the electron excitation from VB to CB, Green line shows the electron excitation from VB to IB, and red line shows BGE excites electrons from the IB states to CB and from NRR level to IB. The dashed line indicates the nonradiative recombination of electrons.

5.2.4 Time-resolved PL Measurement and Determination of Trap Parameters by Rate Equation Analysis

In order to consolidate our qualitative interpretations according to a postulated energy diagram shown in Figure 5.3 and measured lifetime, a quantitative simulation of the TWEPL results was carried out for the most dominant PL increase occurred by the 1.46 eV BGE for the IB and the CB excitations.

To better understand the recombination mechanism in $GaP_{1-x}N_x$ ($x = 0.56\%$), TRPL measurements are performed. Figure 5.4 shows the PL decay profile of $GaP_{1-x}N_x$ ($x = 0.56\%$) at 77 K for CB excitation (470 nm, 2.64 eV). The PL decay curves are fitted by using the same multiexponential function of equation (4.6). In Figure 5.4, the yollow line shows the fitting curve for CB excitaion. The calculated decay times are shown in Table 5.1.

Table 5.1. PL decay time of $GaP_{1-x}N_x$ (x=0.56%) for CB excitasion.

Excitaion (nm)	τ_1 (ns)	τ_2 (ns)	τ_3 (ns)
470 nm	1.13	7.41	596.89

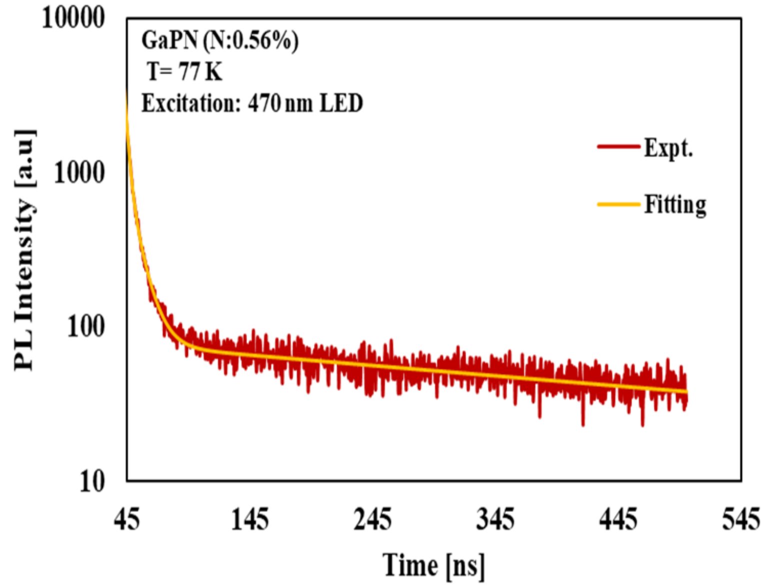

Figure 5.4 PL decay profile of $GaP_{1-x}N_x$ ($x = 0.56\%$) with fitting curve under CB excitation.

The relationship between C_{p1} and N_{t1} is obtained from TRPL measurement by using the same equation (4.8). By using a set of C_{p1} and N_{t1} values, which satisfy equation (4.8), the calculated value of τ_1 matches with experimental value of 1.13 ns. The calculated values of trap parameters are tabulated in Table 5.2.

Table 5.2. Values of C_{p1} and N_{t1} for $GaP_{1-x}N_x$(x=0.56%) determined by TRPL measurement.

B ($cm^3 s^{-1}$)	n_0 (cm^{-3})	C_{p1} ($cm^3 s^{-1}$)	N_{t1} (cm^{-3})
4.33×10^{-11}	8.0×10^{14}	1.0×10^{-5}	8.8×10^{13}

Equations (4.1), (4.2), (4.3), and (4.4) are used for rate equation analysis of $GaP_{1-x}N_x$ ($x = 0.56\%$) sample. The generation rate of AGE (G_1) is calculated experimentally by using equation (4.5). The system of rate equations can be solved numerically and the dependencies of n, p, and f_{t1} on G_2 can be found for the constant parameters of G_1, B, and n_0 and NRR1 dependent parameters C_{n1}, C_{p1}, and N_{t1}. The values of C_{p1} and N_{t1} of $GaP_{1-x}N_x$ ($x = 0.56\%$) are already determined by TRPL measurement. By systematically solving and fitting the results with experimental data, all the NRR parameters are obtained as shown in Table 5.3.

Table 5.3. Trap parameters of the dominant NRR1 center for IB and CB excitation.

Excitaion (nm)	G_1 ($cm^3 s^{-1}$)	B ($cm^3 s^{-1}$)	n_0 (cm^{-3})	C_{n1} ($cm^3 s^{-1}$)	C_{p1} ($cm^3 s^{-1}$)	N_{t1} (cm^{-3})
532	4.8×10^{23}	4.33×10^{-11}	8.0×10^{16}	7.0×10^{-9}	1.0×10^{-5}	8.8×10^{13}
355	3.4×10^{23}	4.33×10^{-11}	8.0×10^{16}	7.0×10^{-9}	1.0×10^{-5}	8.8×10^{13}

Figure 5.5 (a) shows the variation of I_N values as a function of the electron-hole generation rate (G_2) of the 1.46 eV BGE at 77 K under IB excitation with a fixed generation rate of 4.8×10^{23} cm^{-3} s^{-1}. The solid square (orange) and broken (orange) line represent the experimental and simulated data of I_N values respectively. The simulated I_N values exhibit a reasonable agreement with the experimental data. The variation of normalized PL intensity as a function of the electron-hole generation of IB excitation (G_1) at 77 K is calculated by setting $G_2 = 1 \times 10^{13}$ cm^3 s^{-1} for 1.46 eV BGE and keeping all the parameters same as previous calculations. Figure 5.5 (b) shows the depicted results along with experimental results. Here, a set of parameters give the behavioral insight into below-gap states acting as NRR1 center in $GaP_{1-x}N_x$ ($x = 0.56\%$), and there is a reasonable fitting with the experimental data.

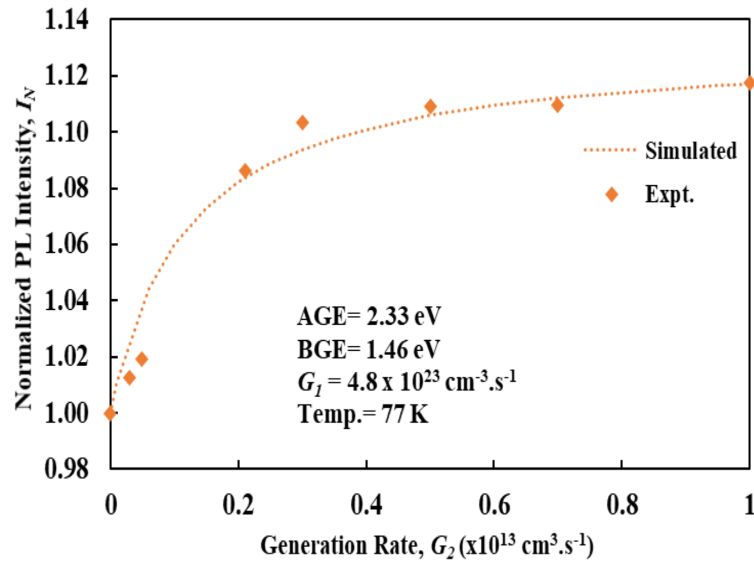

(a)

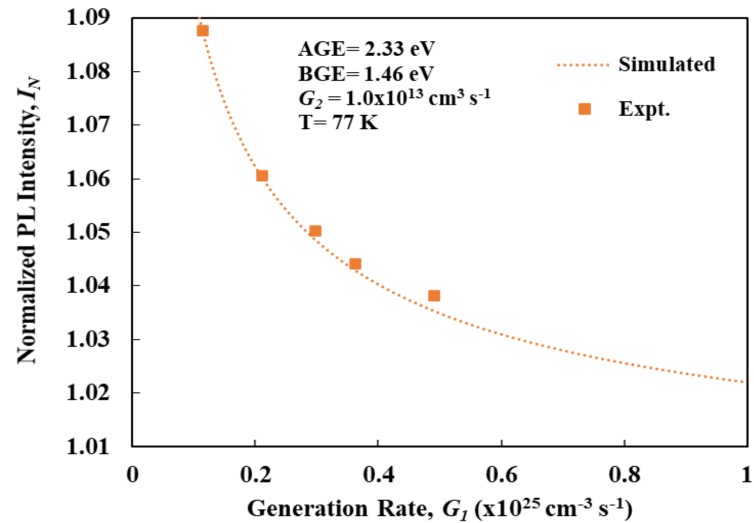

(b)

Figure 5.5 (a) Variation of I_N values as a function of G_2 and (b) Variation of I_N values as a function of G_1 at 77 K for 1.46 eV BGE for IB excitation.

Figure 5.6 (a) shows the variation of I_N values as a function of the electron-hole generation rate (G_2) of the 1.46 eV BGE at 77 K under CB excitation with a fixed generation rate of 3.4×10^{23} cm^{-3} s^{-1}. The solid dot (blue) and broken (blue) line represent the experimental and simulated data, respectively. The influence of I_N values as a function

of electron-hole generation rate of CB excitation (G_1) at 77 K is calculated by setting $G_2 = 1 \times 10^{13}$ cm^3 s^{-1} for 1.46 eV BGE, as shown in Figure 5.6 (b). In the calculation of CB excitation, the value of all NRR1 parameters is as same as calculated in IB excitation. The only difference is in the electron-hole generation rate of AGE and BGE. Although this set of parameters (Table 5.3) shows a reasonable fit with AGE and BGE photon number density dependence under IB and CB excitations, the possibility of another set of parameters should not be ruled out. Actual excitation and recombination processes take place in parallel, and the situation becomes more complex. However, it is clear that the one-level model is valid as the fundamental NRR process for interpreting our experimental results. It gives us a way of detecting and characterizing NRR centers.

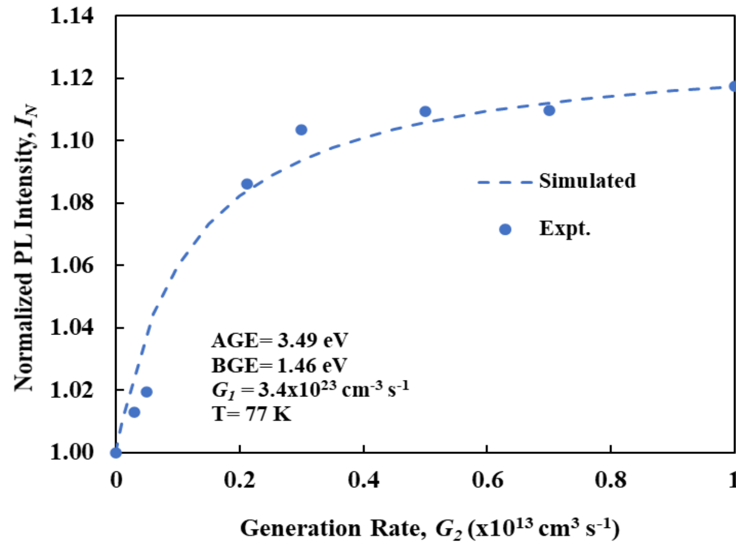

(a)

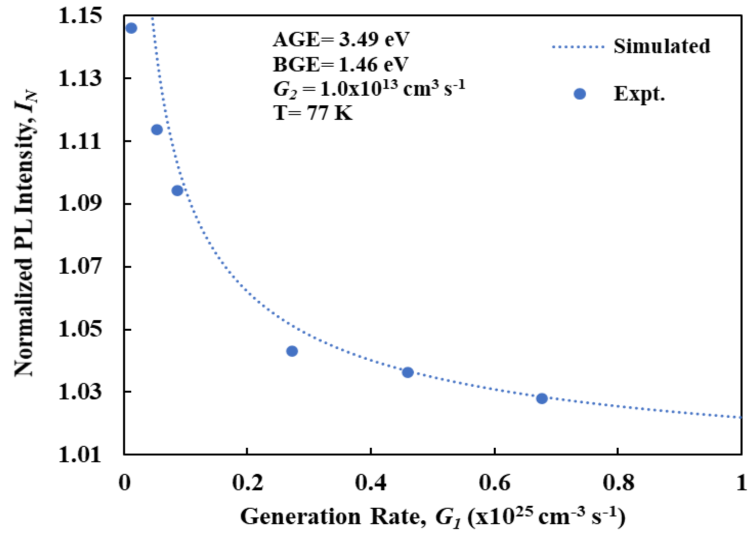

(b)

Figure 5.6 (a) Variation of I_N values as a function of G_2 and (b) Variation of I_N values as a function of G_1 at 77 K for 1.46 eV BGE for CB excitation.

5.3 Conclusion

Defect states acting as NRR centers in $GaP_{1-x}N_x$ ($x = 0.56\%$), were detected and characterized by TWEPL method. To discuss the energy distribution of NRR centers, lasers with photon energies of 0.81 eV, 0.93 eV, 1.17 eV, 1.27 eV, 1.46 eV were provided. All the BGE energies increased PL intensity, which indicates the presence of NRR centers and a secondary excitation from the IB to CB. The most dominant increase was at 1.46 eV BGE both for IB and CB excitation. Depending on the effect of BGE energies, the distribution of NRR centers and NRR process among CB, IB and VB was interpreted in an energy diagram. By combining the result of TRPL with that of TWEPL in a simulation of rate equations, the NRR parameters were evaluated. The rate equations analysis agreed well with the experimental results and justified the phenomenological model consideration for both IB and CB excitation.

CHAPTER 6

CHARACTERIZATION OF NONRADIATIVE RECOMBINATION CENTERS IN GaPN (0.75%)

6.1 Introduction

With continuation of our study of detecting NRR centers in $GaP_{1-x}N_x$ with N concentrations $x = 0.105\%$ and $x = 0.56\%$, here we focus on detection and characterization of NRR centers at $x = 0.75\%$. We observed 70 meV red-shift of peak wavelength and 30 meV broadening of half-width at 77 K with increasing N concentration from 0.105% to 0.56%. Depending on the effect of different BGE energies, an energy diagram on the distribution of NRR centers and NRR process was interpreted. The saturation of PL increase is attributed to the trap-filling effect in NRR centers, which allowed us to modify rate equation. The NRR parameters were evaluated by a qualitative simulation of the modified rate equations of one-level model together with the lifetime determined by TRPL. In continuation of evaluating NRR parameters by rate equation analysis, the addition of TRPL measurement improves accuracy and approaches the determination of NRR parameters.

6.2 Results and Discussion

6.2.1 PL Intensity

PL spectra were measured at 77 K (in liquid N_2) with a variation of AGE excitation power density for both IB and CB excitations as shown in Figure 6.1 (a) and (b). The dominant peak is at 2.10 eV in both cases of the IB and the CB excitations without any change in spectral shape. The small peak at 2.07 eV in the PL spectra is due to the phonon replica.[71] Figure 6.1 (c) shows integrated PL intensity calculated as a function of AGE photon number density for both the IB and the CB excitations. The integrated PL intensity under the IB and the CB excitations increases almost linearly with increasing AGE photon number density. In spite of large difference in absorption coefficient, the integrated PL intensity for the IB excitation is higher than that of the CB at the same AGE photon number density, thus showing a higher emission efficiency of the IB. The fact that the IB excitation

results in higher emission efficiency than the CB excitation gives us an important clue for considering recombination process discussed in 6.2.3.

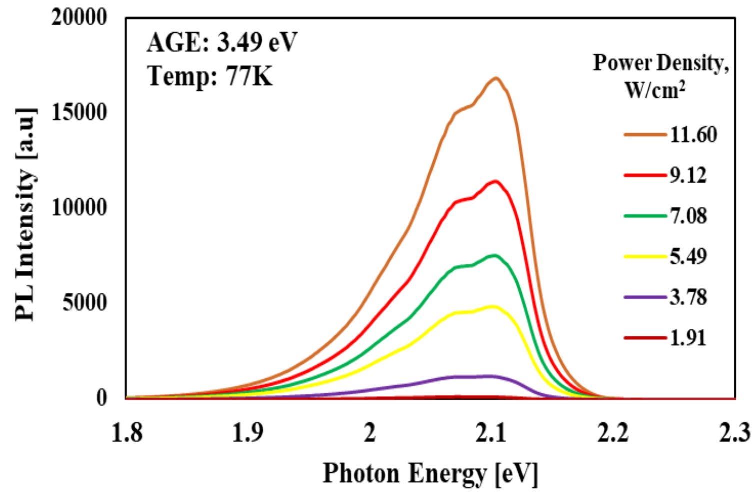

(a)

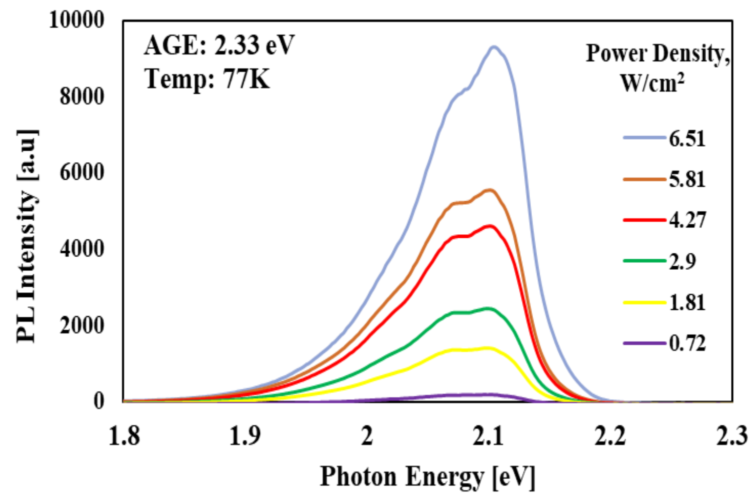

(b)

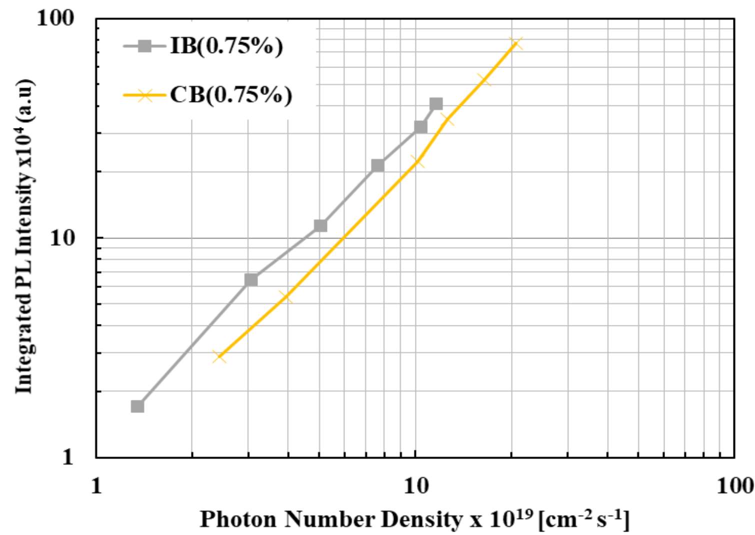

(c)

Figure 6.1 AGE power density dependent PL intensity for a) CB excitation and b) IB excitation. c) Integrated PL intensity for IB and CB excitation.

6.2.2 BGE Dependence of the PL Intensity

In order to know the distribution of NRR centers in $GaP_{1-x}N_x$ ($x = 0.75\%$) sample, the normalized PL intensity (I_N) was measured as a function of the BGE photon number density for five BGE energies as 0.81, 0.93, 1.17, 1.27, and 1.46 eV, respectively. The variation of I_N values as a function of BGE photon number density for the IB excitation is shown in Figure 6.2 (a). Here, the AGE power density was fixed at 5.14 W cm^{-2}. When BGE is superposed over the AGE, the values of I_N increased from unity for all BGE energies. It is observed from Figure 6.2 (a) that the amount of PL increase becomes pronounced with increasing BGE photon number density and gradually tends to be saturated. The most dominant increase of I_N value 1.06 occurred by the 0.93 eV BGE energy with a photon number density of 4.5×10^{18} cm^{-2} s^{-1}. We need to distinguish two BGE processes in our GaPN: one is the BGE process from the IB to the CB, while the other is that from NRR centers to the IB. It can be accomplished by considering the BGE energy dependence. In the former process from the IB to the CB, any final states of BGE from the

IB are allowed as they are allocated inside CB. Thus, the former BGE process from the IB to CB shows no specific BGE energy dependence, but a common part among different BGE energies. On the contrary, a clear BGE energy dependence shown in Figure 6.2 (a) implies that the dominant BGE process is not from the IB to CB, but the process of NRR levels.

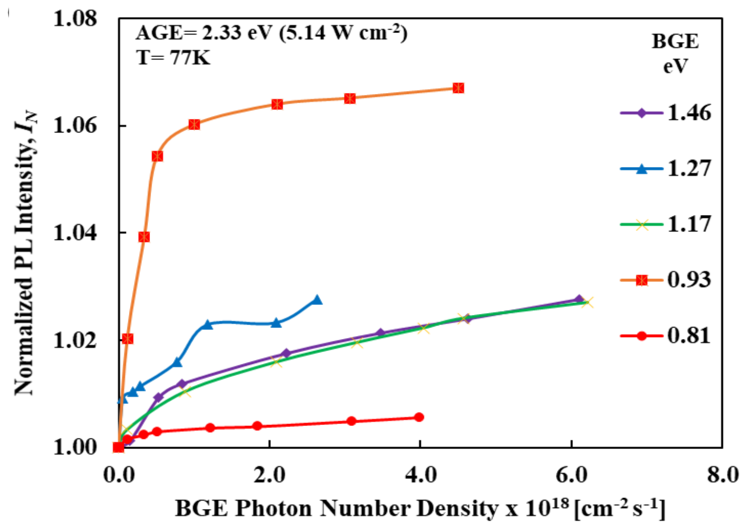

(a)

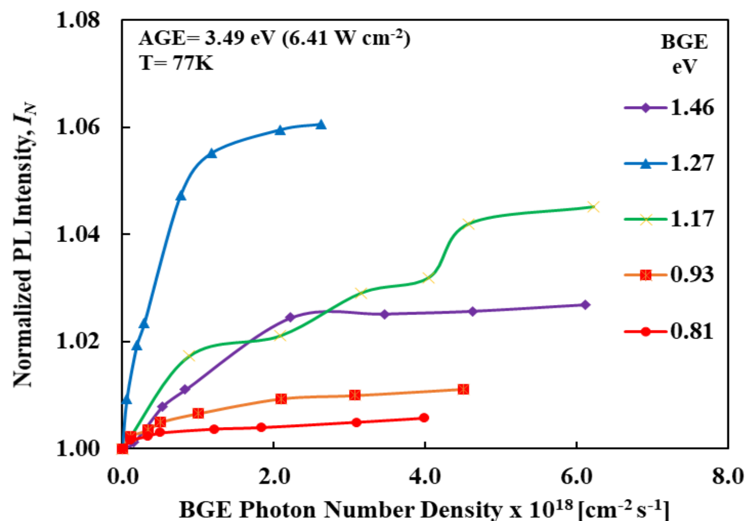

(b)

Figure 6.2 Variation of I_N values as a function of BGE photon number density for (a) IB and (b) CB excitation.

Figure 6.2 (b) shows the variation of I_N values as a function of BGE photon number density for the CB excitation. In this case, the AGE power density was fixed at 6.41 Wcm^{-2}. With the addition of BGE light on the AGE, the values of I_N increased from unity for all BGE energies as same as the IB excitation. It is observed from Figure 6.2 (b) that the normalized PL intensity increases with increasing BGE photon number density and then it shows a saturating tendency at higher photon number density. The most dominant increase of the I_N value 1.06 occurred by the 1.27 eV BGE energy with a photon number density of 2.6×10^{18} cm^{-2} s^{-1}. The increase of I_N values from unity suggests the BGE process again from IB to CB and/or from NRR centers to the IB or CB. A distinct energy dependence shown in Figure 6.2 (b) implies that the dominant BGE process is the latter one. Therefore, our experimental results shown in Figure 6.2 (a) and (b) are effective for characterizing NRR centers in $GaP_{1-x}N_x$ ($x = 0.75\%$).

6.2.3 Characterizations of NRR centers

Figure 6.3 shows a schematic energy diagram of optical excitation and carrier recombination processes which explains the PL intensity increase due to the irradiation of the BGE. In IB excitation, it is observed that the most dominant increased in PL intensity occurred for 0.93 eV BGE according to Figure 6.3 (a). In CB excitation, however, the I_N values due to the 0.93 eV BGE are not dominant. Considering I_N values for all five BGE energies, a NRR level (NRR1) is allocated at 0.93 eV above VB. In IB excitation, the photo-generated electron density in the IB is lower than that in the CB under CB excitation. But the IB emission process in IB excitation is more efficient. It means that NRR rate among CB, IB and VB is lower than the case of CB excitation. Thus, the occupation function of NRR1(f_{t1}) is far less than 1 for the IB excitation. When the BGE light irradiates on the $GaP_{1-x}N_x$ ($x = 0.75\%$) sample, electrons are excited from VB to NRR1 as well as excited from IB to CB. The electron excitation from VB to NRR1 takes place efficiently for 0.93 eV BGE since the energy difference matches for that BGE. Thus, the PL intensity increases distinctly due to electron excitation from VB to NRR1 for 0.93 eV BGE. For CB excitation, higher-density electrons are excited from VB to CB, but major number of electrons of CB relaxes into an extended state, through which they find longer capture

cross section of the NRR1 and other tail states.[31] In such situation much more electrons fall into the NRR1, and its occupation function approaches unity. The BGE from VB to the NRR1 is prohibited due to Pauli exclusion principle. For 1.17 and 1.27 eV BGE, electrons are excited from NRR1 to the IB as well as from the IB to the CB and I_N value become dominant for 1.27 eV BGE. For 1.46 eV BGE, electrons are excited from the NRR1 to the extended state. Some part of electrons in the extended state relaxes into IB and increase the PL intensity, but more electrons find defect levels and recombine nonradiatively. For this phenomenon, the PL intensity increases but its I_N value is lower than those of 1.27 and 1.17 eV. There is a possibility to have a distribution of discrete energy level near the NRR1 level. So, some electrons might be excited from the discrete NRR level to IB for 0.93 and 0.81 eV BGE which is responsible for small increase of I_N value.

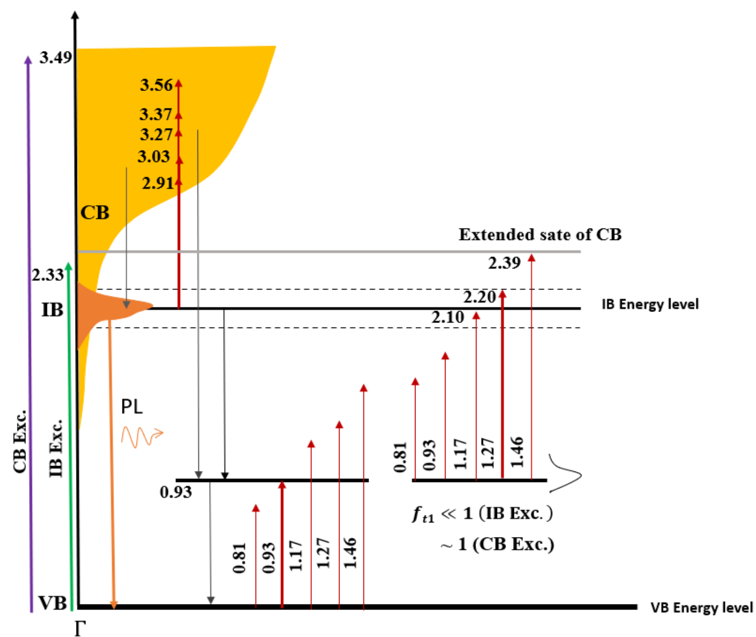

Figure 6.3 Schematic energy diagram of NRR processes in $GaP_{1-x}N_x$ ($x = 0.75\%$) alloy. The spectrum of IB-PL (colored by orange) indicates the position of the IB. Purple line shows the electron excitation from VB to CB, Green line shows the electron excitation from VB to IB, and red line shows BGE excites electrons from the IB states to CB and from VB to NRR level and from NRR to IB.

6.2.4 Time-resolved PL Measurement and Determination of Trap Parameters by Rate Equation Analysis

In order to consolidate our qualitative interpretations according to a postulated energy diagram shown in Figure 6.3 and measured lifetime, a quantitative simulation of the TWEPL results was carried out for the two most dominant PL increase occurred by the 0.93 and 1.27 eV BGE for the IB and the CB excitations, respectively. The modified rate equations for one-level model for IB excitation can be written as, [59,64-66]

$$\frac{dn}{dt} = G_1 - Bnp - nC_{n1}N_{t1}(1 - f_{t1}) = 0; \quad (6.1)$$

$$\frac{dp}{dt} = G_1 - Bnp - pC_{p1}N_{t1}f_{t1} + G_2N_{t1}(1 - f_{t1}) = 0; \quad (6.2)$$

$$\frac{df_{t1}}{dt} = nC_{n1}(1 - f_{t1}) - pC_{p1}f_{t1} + G_2(1 - f_{t1}) = 0; \quad (6.3)$$

where the radiative recombination coefficient B is measured as 4.33×10^{-11} cm^3 s^{-1} for $GaP_{1-x}N_x$ ($x = 0.75\%$) sample. The generation rate of the AGE (G_1) is calculated experimentally by using equation (4.5).

Figure 6.4 shows the PL decay profile of $GaP_{1-x}N_x$ ($x = 0.75\%$) at 77 K for CB excitation (470 nm, 2.64 eV). The red line shows the fitting curve for CB excitaion. The PL decay times were calculated by same way as privious samples and are shown in Table 6.1.

Table 6.1. PL decay time of $GaP_{1-x}N_x$(x=0.75%) for CB excitasion.

Excitaion (nm)	τ_1 (ns)	τ_2 (ns)	τ_3 (ns)
470 nm	1.58	8.79	537.81

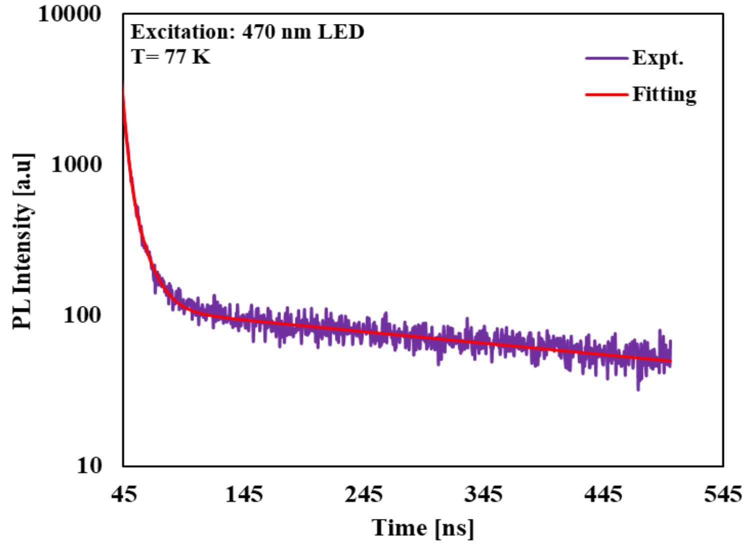

Figure 6.4 PL decay profile of $GaP_{1-x}N_x$ ($x = 0.75\%$) with fitting curve under CB excitation.

By using the same equation (4.8) as used in previous samples in this research, a relationship between C_{p1} and N_{t1} is obtained from TRPL measurement. By using a set of C_{p1} and N_{t1} values, which satisfy equation (4.8), the calculated value of τ_1 matches with experimental value of 1.58 ns. The calculated values of trap parameters are tabulated in Table 6.2.

Table 6.2. Values of C_{p1} and N_{t1} for $GaP_{1-x}N_x$(x=0.75%) determined by TRPL measurement.

B ($cm^3 s^{-1}$)	n_0 (cm^{-3})	C_{p1} ($cm^3 s^{-1}$)	N_{t1} (cm^{-3})
4.33×10^{-11}	3.0×10^{16}	3.0×10^{-6}	2.1×10^{14}

The system of rate equations can be solved numerically and the dependencies of n, p, and f_{t1} on G_2 can be found for the constant parameters of G_1, B, and n_0 and NRR1 dependent parameters C_{n1}, C_{p1}, and N_{t1}. The values of C_{p1} and N_{t1} of $GaP_{1-x}N_x$ ($x = 0.75\%$) are already determined by TRPL measurement. By systematically solving and fitting the results with experimental data, all the NRR parameters are obtained as shown in Table 6.3.

Table 6.3. Trap parameters of the dominant NRR1 center for IB and CB excitation.

Excitaion (nm)	G_1 ($cm^3 s^{-1}$)	B ($cm^3 s^{-1}$)	n_0 (cm^{-3})	C_{n1} ($cm^3 s^{-1}$)	C_{p1} ($cm^3 s^{-1}$)	N_{t1} (cm^{-3})
532	3.4×10^{23}	4.33×10^{-11}	3.0×10^{16}	1.0×10^{-9}	3.0×10^{-6}	2.1×10^{14}
355	2.9×10^{23}	4.33×10^{-11}	3.0×10^{16}	1.0×10^{-9}	3.0×10^{-6}	2.1×10^{14}

Figure 6.5 (a) shows the variation of I_N and f_{t1} values as a function of the electron-hole generation rate (G_2) of the 0.93 eV BGE at 77 K under IB excitation with a fixed generation rate of 3.4×10^{23} cm^{-3} s^{-1}. The solid square (orange) and broken (orange) line represent the experimental and simulated data of I_N values respectively and the solid gray line represent the simulated data of f_{t1} values. The simulated I_N values exhibit a reasonable agreement with the experimental data. At lower G_2, f_{t1} values are very near to zero and approaches unity as I_N values shows saturation. The variation of normalized PL intensity as a function of the electron-hole generation of IB excitation (G_1) at 77 K is calculated by setting $G_2 = 1 \times 10^{13}$ cm^3 s^{-1} for 0.93 eV BGE and keeping all the parameters same as previous calculations. Figure 6.6 (b) shows the depicted results along with experimental results. Here, a set of parameters give the behavioral insight into below-gap states acting as NRR1 center in $GaP_{1-x}N_x$ ($x = 0.75\%$), and there is a reasonable fitting with the experimental data.

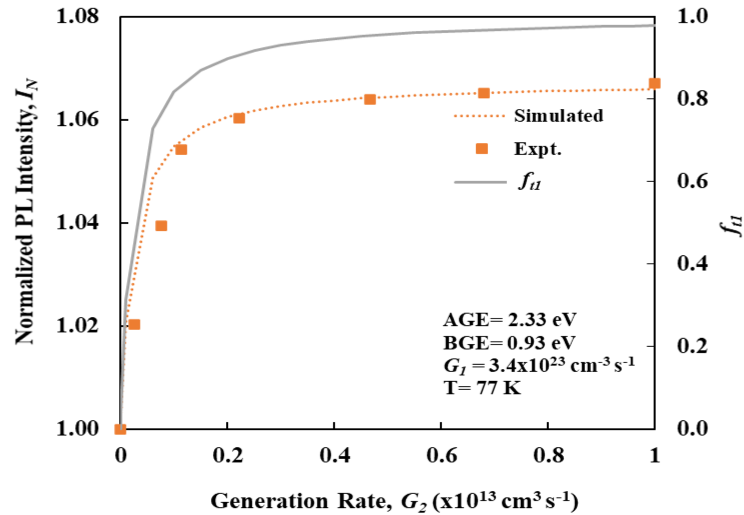

(a)

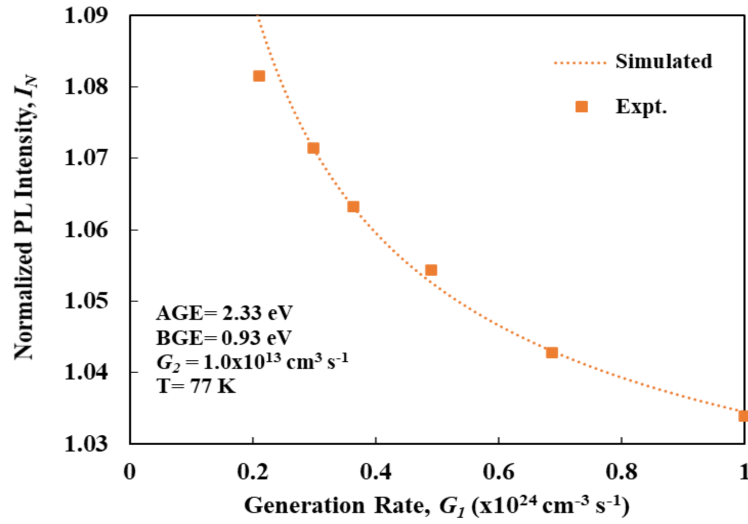

(b)

Figure 6.5 (a) Variation of I_N and f_{t1} values as a function of G_2 and (b) Variation of I_N values as a function of G_1 at 77 K for 0.93 eV BGE for IB excitation.

The rate equations for one-level model for CB excitation are changed to,

$$\frac{dn}{dt} = G_1 - Bnp - nC_{n1}N_{t1}(1 - f_{t1}) + G_2N_{t1}f_{t1} = 0; \quad (6.4)$$

$$\frac{dp}{dt} = G_1 - Bnp - pC_{p1}N_{t1}f_{t1} = 0; \quad (6.5)$$

$$\frac{df_{t1}}{dt} = nC_{n1}(1 - f_{t1}) - pC_{p1}f_{t1} - G_2f_{t1} = 0; \quad (6.6)$$

Figure 6.6 (a) shows the variation of I_N and f_{t1} values as a function of the electron-hole generation rate (G_2) of the 1.27 eV BGE at 77 K under CB excitation with a fixed generation rate of 2.9×10^{23} cm^{-3} s^{-1}. The solid dot (blue) and broken (blue) line represent the experimental and simulated data respectively and the solid gray line represent the simulated data of f_{t1} values. Since much more electrons fall from higher bands to NRR1 in CB excitation, f_{t1} values are very near to unity at lower G_2. With the increase of the BGE, electrons excited from NRR1 to the IB and the probability of occupied state at NRR1

approaches zero as I_N values shows saturation. The influence of I_N values as a function of electron-hole generation rate of CB excitation (G_1) at 77 K is calculated by setting $G_2 = 1 \times 10^{12}$ cm^3 s^{-1} for 1.27 eV BGE, as shown in Figure 6.6 (b). In the calculation of CB excitation, the value of all NRR1 parameters is as same as calculated in IB excitation. The only difference is in the electron-hole generation rate of AGE and BGE. Although this set of parameters (Table 6.3) shows a reasonable fit with AGE and BGE photon number density dependence under IB and CB excitations, the possibility of another set of parameters should not be ruled out. Actual excitation and recombination processes take place in parallel, and the situation becomes more complex. However, it is clear that the one-level model is valid as the fundamental NRR process for interpreting our experimental results. It gives us a way of detecting and characterizing NRR centers.

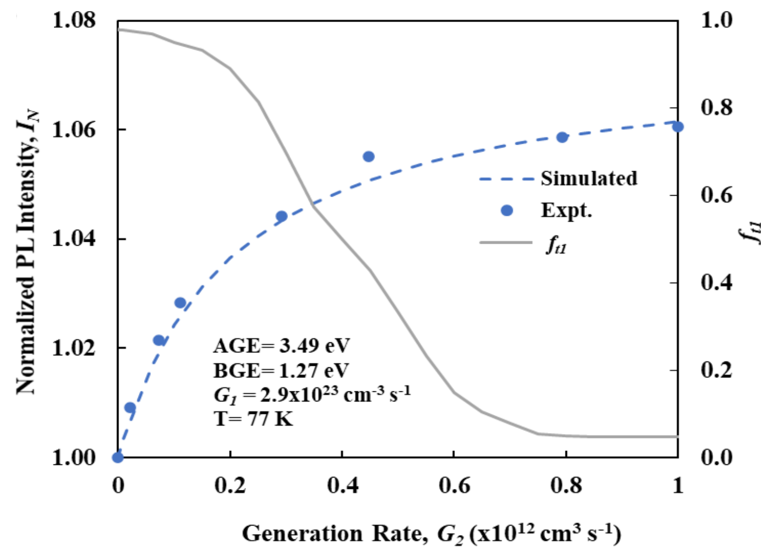

(a)

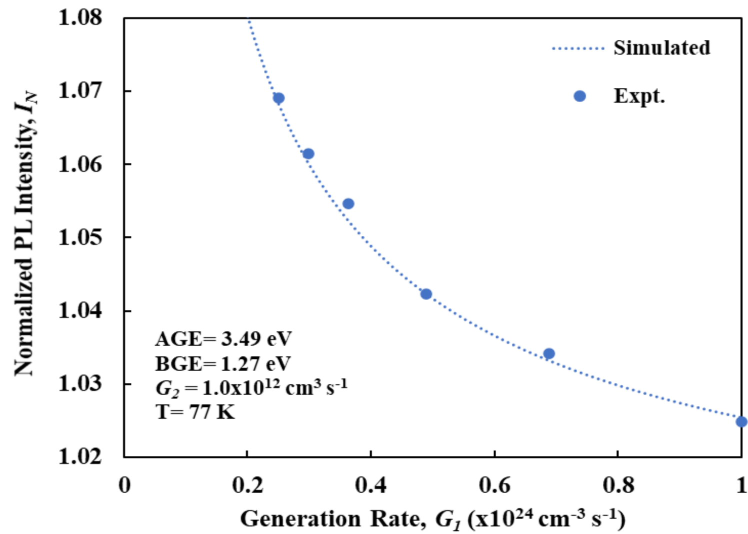

(b)

Figure 6.6 (a) Variation of I_N and f_{t1} values as a function of G_2 and (b) Variation of I_N values as a function of G_1 at 77 K for 1.27 eV BGE for CB excitation.

6.3 Conclusion

Defect states acting as NRR centers in $GaP_{1-x}N_x$ ($x = 0.75\%$), were detected and characterized by TWEPL method. All the BGE energies increased PL intensity, which indicates the presence of NRR centers and a secondary excitation from the IB to CB. The most dominant increase was at 0.93 eV BGE for IB excitation and at 1.27 eV BGE for CB excitation. Depending on the effect of BGE energies, the distribution of NRR centers and NRR process among CB, IB and VB was interpreted in an energy diagram. By combining the result of TRPL with that of TWEPL in a simulation of rate equations, the NRR parameters were evaluated. Here, a modified one-level model was proposed to clarify the saturation phenomenon of PL increase due to trap-filling of electrons in the NRR level, which showed reasonable agreement between experimental results. A set of NRR parameters that give a qualitative insight in the samples has been evaluated by systematically solving the rate equations and fitting the results with the experiment.

CHAPTER 7

COMPARISON OF NONRADIATIVE RECOMBINATION PARAMETERS OF GaPN SAMPLES WITH N CONCENTRATION OF 0.105. 0.56 AND 0.75%

7.1 Introduction

Nonradiative recombination (NRR) centers in three different GaPN samples with three different nitrogen concentration of 0.105%, 0.56%, and 0.75% have been detected and characterized by TWEPL method. All three samples were grown by same Metal Organic Chemical Vapor Deposition (MOCVD) technique. On lower N concentration region, the PL spectrum of GaPN originates from isoelectronic trap and NN_i pairs and it merges to that of IB with increasing N concentration. Since the carrier recombination process via IB is different due to a slight change in N concentration, it is demonstrated that the amount of N has a large effect on the physical properties. Characterization of NRR levels and make a comparative study with different N concentration samples is important to predict the optimum condition of GaPN alloy for advancing the application of IBSCs.

7.2 Results and Discussion

7.2.1 N Concentration Dependence of PL Intensity

Figure 7.1 shows the PL spectra of $GaP_{1-x}N_x$ samples for three different N concentration of $x = 0.105, 0.56$ and 0.75% at 77 K. With increasing *N* concentration, the PL spectrum of GaPN transforms from superposition of discrete peaks to a broader PL band corresponding to the formation of IB.[18, 72-74] The increase in the N concentration causes a shift of the IB emission toward lower energies as coincided with previous research.[36,43]

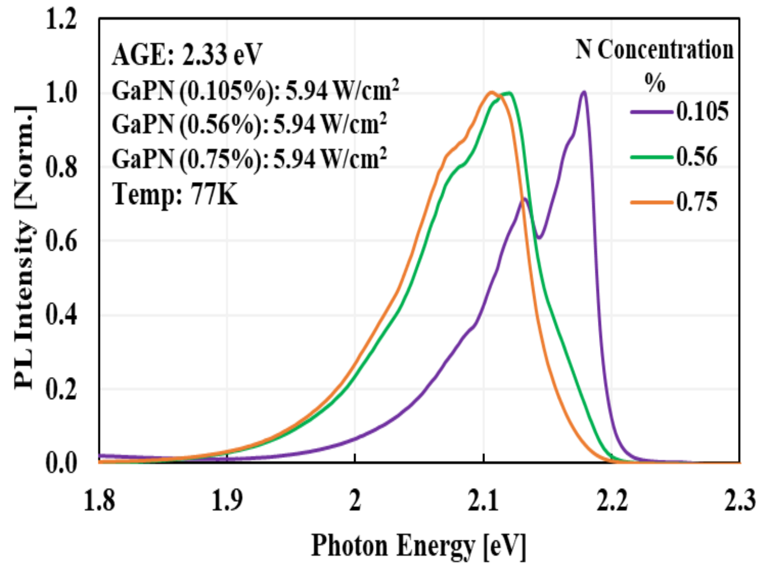

Figure 7.1 PL spectra of $GaP_{1-x}N_x$ samples (x= 0.105, 0.56 and 0.75%) at 77 K.

Figure 7.2 (a), (b) and (c) show the PL intensity for CB and IB excitation for three GaPN samples. Figure 7.3 shows the integrated PL intensity under the IB and the CB excitations increases almost linearly with increasing AGE photon number density for all three samples. In every case of GaPN samples the PL intensity of IB excitation is greater than the PL intensity of CB excitation. It is considered that the discreate energy levels of tail state of CB act as nonradiative recombination centers. A part of excited electrons in CB excitation recombines nonradiatively through this tail state NRR centers. This phenomenon decreases the PL intensity in CB excitation. The PL intensity of $GaP_{1-x}N_x$ $(x = 0.56\%)$ sample shows high luminescence among three samples.

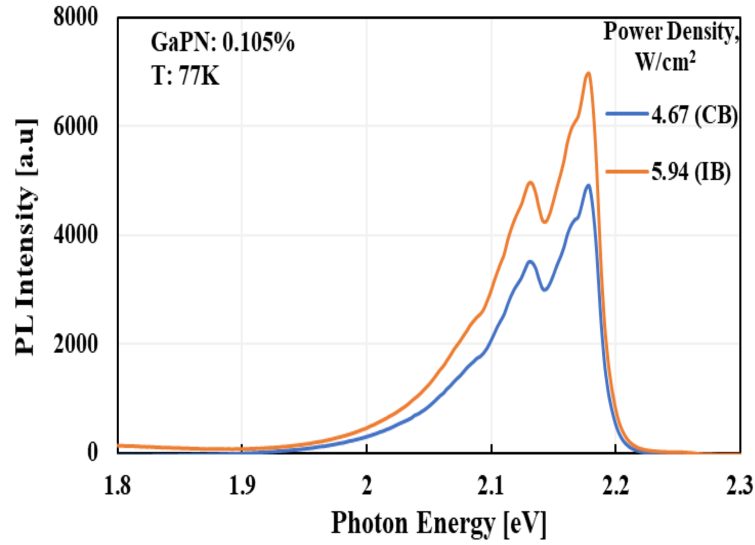

(a)

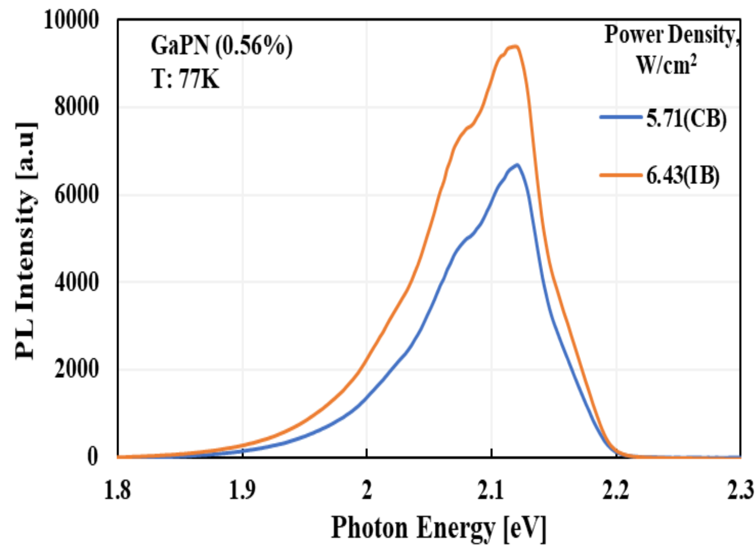

(b)

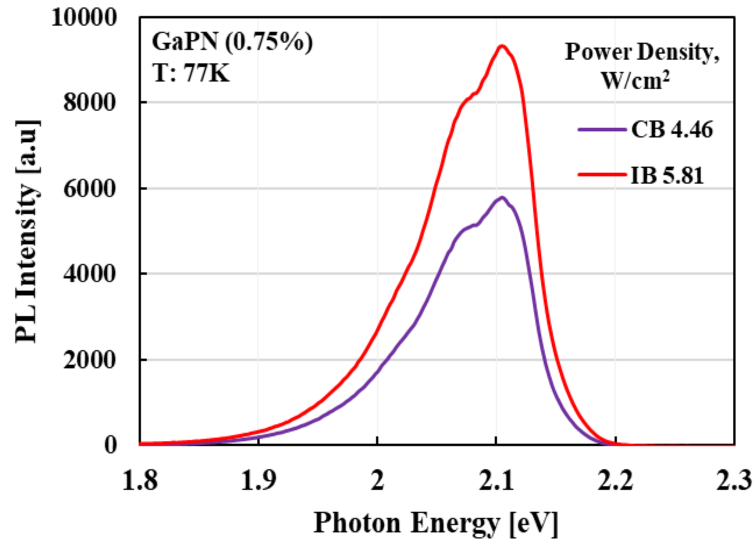

(c)

Figure 7.2 PL intensity for IB and CB excitation for (a) GaPN (0.105%), (b) GaPN (0.56%), and (c) GaPN (0.75%) samples.

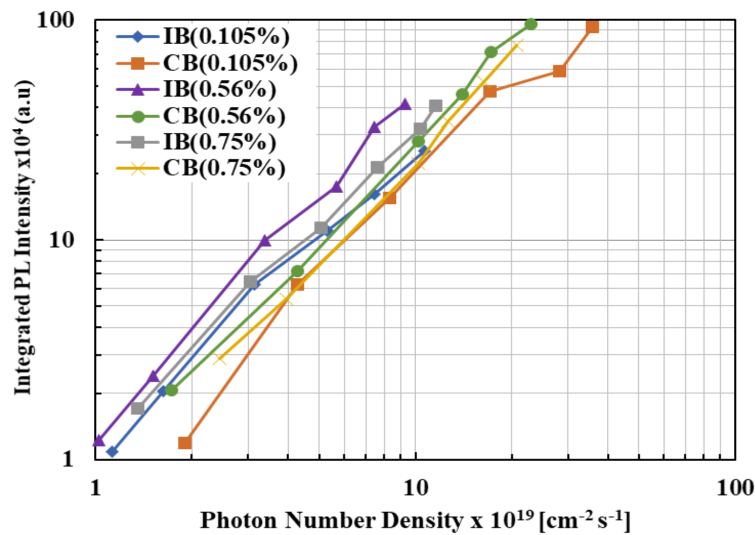

Figure 7.3 Integrated PL intensity for IB and CB excitation with AGE photon number density.

7.2.2 BGE Effect

When a GaPN sample with a N concentration of 0.105% was measured, IB emission consisting of multiple constituents was obtained. Then, when BGE light was irradiated by the TWEPL method, the IB emission intensity increased. It is considered that this is because the electron increase of IB via the NRR level was caused by BGE light. Depending on the effect of different BGE energies, an energy diagram on the distribution of NRR centers and NRR process was interpreted. Furthermore, when a sample with a N concentration of 0.56% was measured, IB emission with different shapes and luminous efficiencies was obtained in the lower energy region. We observed 70 meV red-shift of peak wavelength and 30 meV broadening of half-width at 77 K with increasing N concentration from 0.105% to 0.56%. This is because a huge bandgap bowing occurs as the N concentration increases. Then, when BGE light was irradiated, the IB emission intensity increased as in the sample described above. The PL intensity is increased for all five BGE sources of 0.81, 0.93, 1.17, 1.27, and 1.46 eV, whereas in the sample with N concentration of 0.105%, such a clear tendency was not shown, and different BGE energy dependence was observed. This is because the energy distribution is different in each N concentration sample, and different carrier recombination processes can be considered for each. When a sample with a N concentration of 0.75% was measured, IB emission shapes and luminous efficiencies was not so much different from the previous GaPN (0.56%) sample. There was a very little peak sifting toward the lower energy region. The PL intensity is increased for all five BGE sources of 0.81, 0.93, 1.17, 1.27, and 1.46 eV. However, the most dominant increase was at 0.93 eV BGE for IB excitation and 1.27 eV for CB excitation. This phenomenon implies that the energy distribution and the carrier recombination process are different in each N concentration sample. The recombination model has been considered according to the experimental results.

7.2.3 Time-resolved PL Measurement

To better understand the recombination mechanism in $GaP_{1-x}N_x$ Time-resolve Photoluminescence (TRPL) measurements are performed. Figure 7.4 shows the PL decay profile of $GaP_{1-x}N_x$ ($x = 0.105\%, 0.56\%, \text{and } 0.75\%$) samples at 77 K for CB excitation (470 nm, 2.64 eV). The calculated decay times are shown in Table 7.1. The experimental

results show that the nonradiative decay time τ_1 is highest for $GaP_{1-x}N_x$ ($x = 0.105\%$) and lowest for $GaP_{1-x}N_x$ ($x = 0.56\%$) sample.

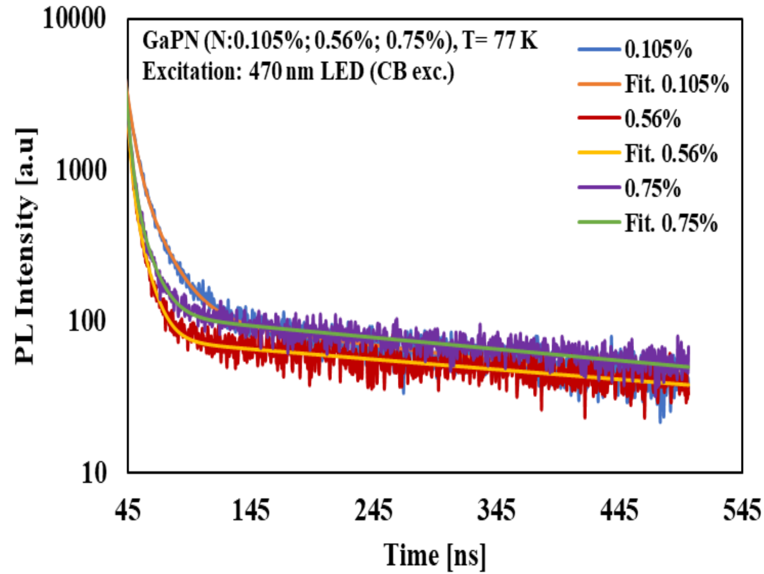

Figure 7.4 PL decay profile of $GaP_{1-x}N_x$ ($x = 0.105\%, 0.56\%, \text{and } 0.75\%$) samples with fitting curve under CB excitation.

Table 7.1. PL decay time for CB excitasion.

Sample	Excitaion (nm)	τ_1 (ns)	τ_2 (ns)	τ_3 (ns)
GaPN (0.105%	470	3.27	17.61	576.59
GaPN (0.56%)	470	1.13	7.81	596.81
GaPN (0.75%)	470	1.58	8.79	537.81

7.2.4 Comparison of NRR parameters

Figure 7.5 shows the schematic energy band diagram of three samples (BGE effect of all the three samples is explained by three different but have common base energy diagram of one-level model Figure 4.6(P.32), Figure 5.3 (P.43) and Figure 6.3 (P.54)). For $GaP_{1-x}N_x$ ($x = 0.105\%$) sample the effect of BGE energies depends also on the AGE excitation power density through a shift of Fermi energy in the forbidden energy gap and the Fermi energy is higher than the NRR energy level both for IB and CB excitation. A

huge bandgap bowing occurs as the N concentration increases. For $GaP_{1-x}N_x$ ($x = 0.56\%$) sample, the Fermi energy is also higher than the NRR energy level. Since the most dominant I_N value for IB and CB is different for $GaP_{1-x}N_x$ ($x = 0.56\%$) sample, the energy diagram is considered in a different way in this case. For IB excitation the Fermi energy is lower than the NRR energy level and electrons excite from VB to NRR level for adding 0.93 eV BGE with IB excitation. The Fermi energy is higher than NRR level for CB excitation and electrons excite from NRR to IB for 1.27 eV BGE. Table 7.2 shows the comparison of results of three GaPN samples obtained by TRPL measurement and rate equation analysis. The NRR parameters are evaluated by combining the results of TRPL measurement and rate equation analysis. It is observed that the defect density of $GaP_{1-x}N_x$ ($x = 0.56\%$) sample is lower among three different samples.

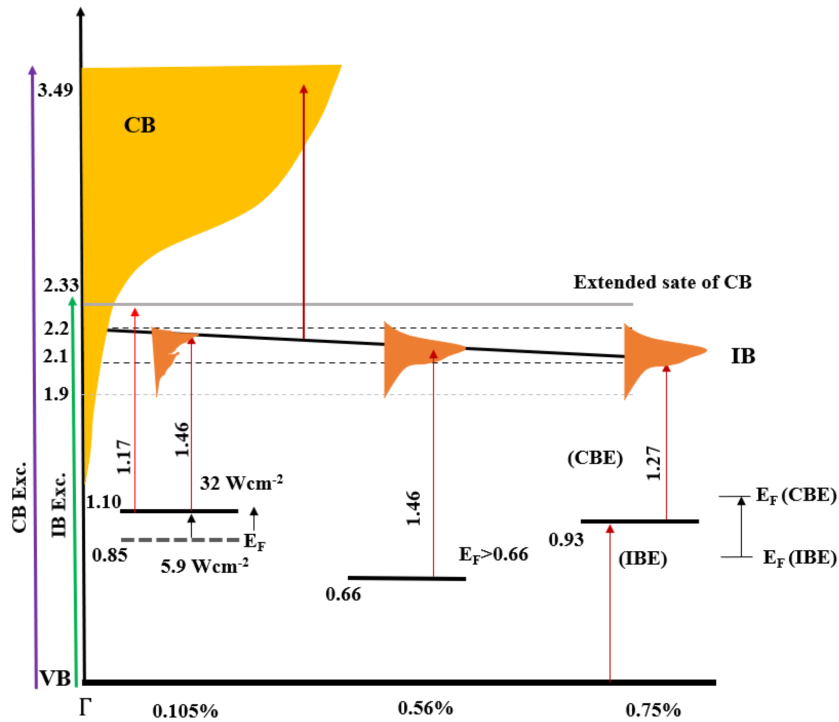

Figure 7.5 Schematic energy band diagram of three samples. The spectrum of IB-PL (colored by orange) indicates the position of the IB. Purple line shows the electron excitation from VB to CB, Green line shows the electron excitation from VB to IB, and red line shows BGE excites electrons from the IB states to CB and from NRR level to IB.

Table 7.2 Comparison of the results of GaPN samples obtained by the rate equation analysis.

Sample	I_N due to superposition of BGE over AGE	Results explained by	Defect density obtained by rate equation analysis
GaPN (0.105%)	Increase	One-level	$N_{t1} = 1.1 \times 10^{14}$ cm^{-3}
GaPN (0.56%)	Increase	One-level	$N_{t1} = 8.8 \times 10^{13}$ cm^{-3}
GaPN (0.75%)	Increase	One-level	$N_{t1} = 2.1 \times 10^{14}$ cm^{-3}

7.3 Conclusion

It is observed from experimental results that with increasing N concentration, the PL spectrum of $GaP_{1-x}N_x$ transforms from superposition of discrete peaks to a broader PL band corresponding to the formation of IB. The increase in the N concentration causes a shift of the IB emission toward lower energies. In order to better understand the recombination mechanism in $GaP_{1-x}N_x$ TRPL measurements have been performed. The experimental results show that the nonradiative decay time τ_1 is highest for $GaP_{1-x}N_x$ ($x = 0.105\%$) and lowest for $GaP_{1-x}N_x$ ($x = 0.56\%$) sample. The evaluated NRR parameters by TRPL measurement and rate equation analysis of three samples shows that the defect density of $GaP_{1-x}N_x$ ($x = 0.56\%$) sample is lower among three different N concentration samples of $GaP_{1-x}N_x$. For actual application of GaPN alloy for IBSC, the Fermi energy level should be very near or inside the IB. In such case VB to IB excitation disappears. Among three samples $GaP_{1-x}N_x$ ($x = 0.56\%$) shows higher emission efficiency with low NRR level. The reduction of defect levels inside the forbidden gap is also important in order to raise the Fermi level up to IB. However, to find the best condition of GaPN alloy for IBSC more samples with higher N concentration should be investigated.

CHAPTER 8
SUMMARY AND FUTURE DIRECTIONS

8.1 Summary

Nonradiative recombination (NRR) centers in three different GaPN samples: $GaP_{1-x}N_x$ (x= 0.105, 0.56 and 0.75%) , grown by MOCVD method, have been detected and characterized by TWEPL method. From the experimental results following conclusions are drawn:

(a) The temperature-dependent PL spectra of $GaP_{1-x}N_x$ ($x = 0.105\%$) between 5 K and 80 K shows that the PL spectrum at 5 K consists of NN_1 (2.18 eV), NN_3 (2.26 eV), NN_4 (2.28 eV) and their phonon replicas. The PL spectra of IB showed a shift toward lower energy-side with increasing temperature. The temperature effect due to BGE irradiation on sample was eliminated by immersing it in liquid N_2 and the TWEPL method revealed the presence of NRR centers in $GaP_{1-x}N_x$ ($x = 0.105\%$). According to the experimental results, two dominant peaks are found at 2.13 and 2.18 eV at 77 K and the PL intensity increased with increasing the AGE power density. The integrated PL intensity for the IB excitation is higher than that of the CB at the same AGE photon number density, thus showing a higher emission efficiency of the IB. Depending on the excitation energies of BGE, different contribution of one-level model and two-level model took place for CB and IB excitation. The effect of BGE energies depends also on the AGE excitation power density through a shift of Fermi energy in the forbidden energy gap. These results are successfully interpreted by a distribution of NRR centers and NRR process among CB, IB and VB by using TWEPL method. By combining the result of TRPL with that of TWEPL in a simulation of rate equations, the NRR parameters were evaluated. The addition of TRPL measurement improves accuracy and is important toward a quantitative determination of NRR parameters in order to optimize IBSCs.

(b) The PL spectrum of $GaP_{1-x}N_x$ ($x = 0.56\%$) transforms from superposition of discrete peaks to a broader PL band corresponding to the formation of IB. The dominant

peak is at 2.12 eV in both cases of the IB and the CB excitations. The integrated PL intensity under the IB and the CB excitations increases almost linearly with increasing AGE photon number density and is higher than that of the CB at the same AGE photon number density, thus showing a higher emission efficiency of the IB. All the BGE energies increased PL intensity, which indicates the presence of NRR centers and a secondary excitation from the IB to CB. The most dominant increase of PL intensity was at 1.46 eV BGE both for IB and CB excitation. Depending on the effect of BGE energies, the distribution of NRR centers and NRR process among CB, IB and VB was interpreted in an energy diagram. By combining the result of TRPL with that of TWEPL in a simulation of rate equations, the NRR parameters were evaluated.

(c) The experimental results of $GaP_{1-x}N_x$ ($x = 0.75\%$) shows that the dominant peak of PL intensity is at 2.10 eV in both cases of the IB and the CB excitations without any change in spectral shape. The integrated PL intensity under the IB and the CB excitations increases almost linearly with increasing AGE photon number density and is higher than that of the CB at the same AGE photon number density. All the BGE energies increased the PL intensity, which indicates the presence of NRR centers and a secondary excitation from the IB to CB. The most dominant increase was at 0.93 eV BGE for IB excitation and at 1.27 eV BGE for CB excitation. Depending on the effect of BGE energies, the distribution of NRR centers and NRR process among CB, IB and VB was interpreted in an energy diagram. By combining the result of TRPL with that of TWEPL in a simulation of rate equations, the NRR parameters were evaluated. Here, a modified one-level model was proposed to clarify the saturation phenomenon of PL increase due to trap-filling of electrons in the NRR level, which showed reasonable agreement between experimental results.

(d) It is observed from experimental results that with increasing N concentration, the PL spectrum of $GaP_{1-x}N_x$ transforms from superposition of discrete peaks to a broader PL band corresponding to the formation of IB. The increase in the N concentration causes a shift of the IB emission toward lower energies. We observed 70 meV red-shift of peak wavelength and 30 meV broadening of half-width at 77 K with increasing N concentration from 0.105% to 0.56%. This is because a huge bandgap bowing occurs as the N concentration increases. When BGE light was irradiated on $GaP_{1-x}N_x$ (x=0.56 and 0.75%)

samples, the PL intensity is increased for all five BGE, whereas in the sample with a N concentration of 0.105%, such a clear tendency was not shown for all BGE lights, and different BGE energy dependence was observed. This is because the energy distribution of NRR centers is different in each sample, and different carrier recombination processes can be considered for each sample. The evaluated NRR parameters by TRPL measurements and rate equation analysis of three samples shows that the defect density of $GaP_{1-x}N_x$ ($x = 0.56\%$) sample is the lowest among three samples. The experimental results shows that $GaP_{1-x}N_x$ ($x = 0.56\%$) sample has the highest emission efficiency with a low NRR density.

It was found from the evaluation that the energy distribution of the carrier recombination process via IB was different due to a slight change in N concentration. For actual application of GaPN alloy for IBSC, the Fermi level should be very near or inside the IB. The reduction of the defect density inside the forbidden gap is also important to raise the Fermi level up to IB. This work also implies that the combination of TRPL results with TWEPL is important to improve the accuracy toward quantitative determination of NRR parameters. However, more samples with higher N concentrations should be investigated to find the best condition of GaPN alloys for the application of IBSC. Considering the detection sensitivity, merit of non-contacting and non-destructive measurement, the way of utilizing the IB luminescence as a probe of characterizing defect levels is beneficial not only for GaPN but also InAs/GaAs, N δ-doped GaAs superlattice and other IB materials.

8.2 Future Directions

Although significant research work has been performed for different samples by TWEPL method, there are many defects related properties which are unsolved and require further investigation. The following research work can be done to obtain more defect related information from the promising IBSC materials.

i. We have characterized the NRR centers in GaPN samples with three different N concentrations for both the CB and IB excitation. The study of other samples with

more different N concentration can provide important information about the spatial distribution and origin of defect level.

ii. We have characterized the NRR centers in GaPN samples grown by MOCVD method. The study of other samples with different growth techniques can provide important information about the spatial distribution and origin of defect level.

iii. The optical characterization of TWEPL together with electrical characterization like DLTS, DLOS, etc. can provide more useful information about the spatial distribution and origin of defect level.

iv. The investigation of the energy distribution of NRR centers can be done by using the tunable and/or different BGE energy sources. This may provide intensive information about the NRR properties of IBSC materials

APPENDIX

A.1 Calibration of different BGE sources output power

Calibration of different BGE sources is presented in the following Figures:

BGE: 850 nm (1.46 eV)

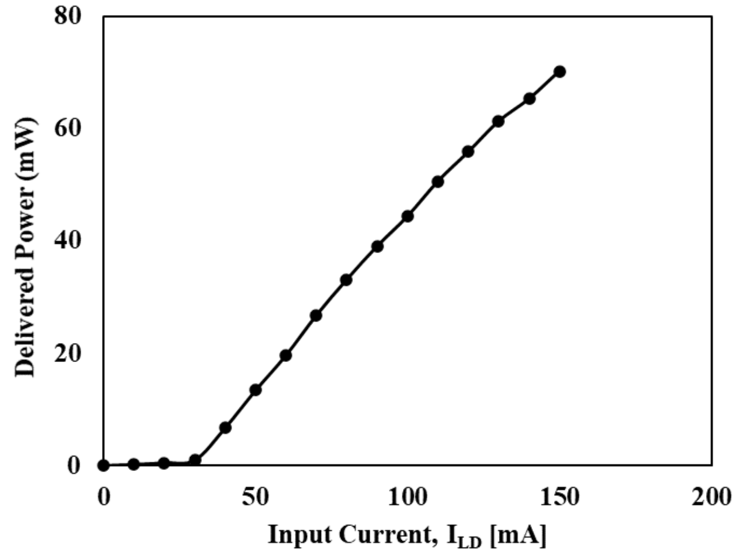

Figure A.1 Calibration of the 850 nm (1.46 eV) laser.

BGE: 980 nm (1.27 eV)

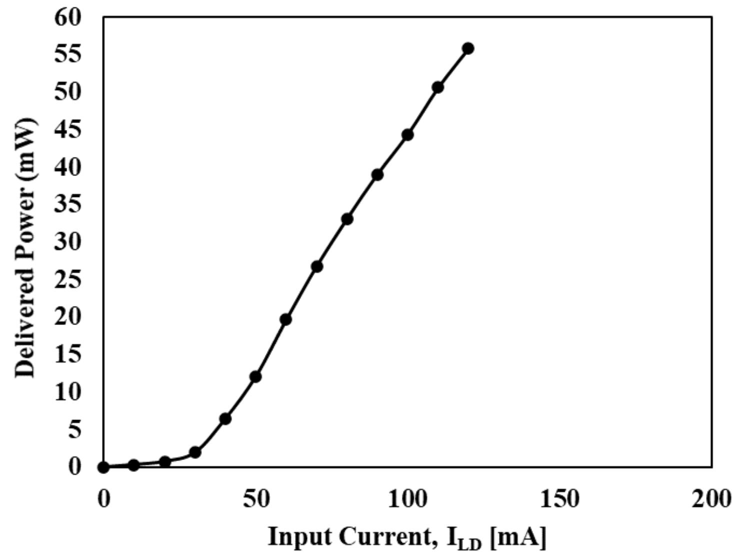

Figure A.2 Calibration of the 980 nm (1.27 eV) laser.

BGE: 1064 nm (1.17 eV)

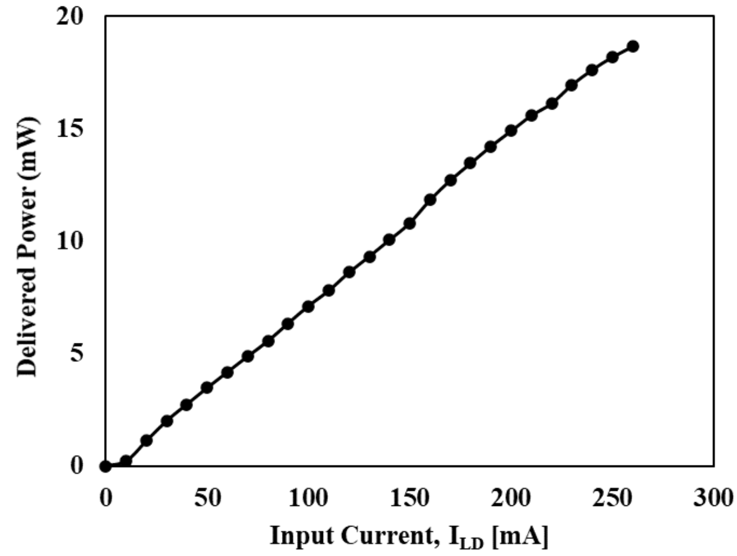

Figure A.3 Calibration of the 1064 nm (1.17 eV) laser.

BGE: 1550 nm (0.81 eV)

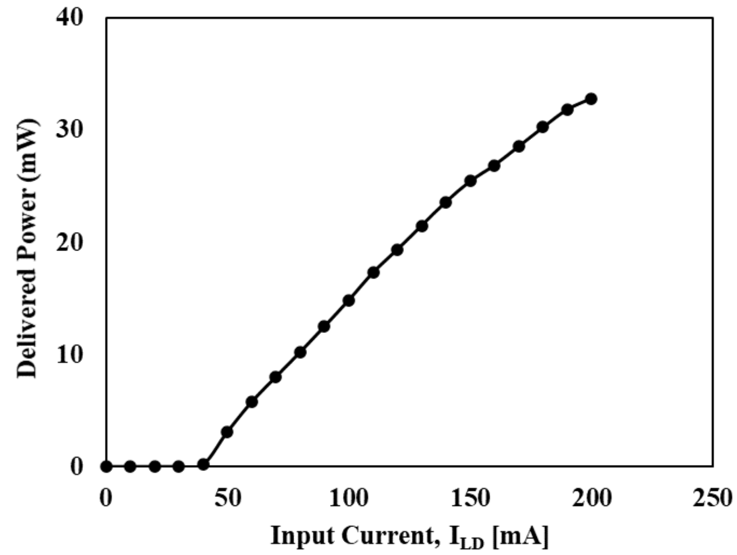

Figure A.4 Calibration of the 1550 nm (0.81 eV) laser.

A.2 Beam parameters of different laser sources

Beam diameter of different lasers was measured by using the knife edge method. The beam parameters are summarized below:

Table A.1 Beam parameters of different lasers

Sources	Lasers	Beam Diameter [mm]	Beam Cross-section [mm^2]
AGE (CB)	355 nm (3.49 eV)	0.15	0.0177
AGE (IB)	532 nm (2.33 eV)	0.225	0.049
BGE	850 nm (1.46 eV)	1.05	0.865
BGE	980 nm (1.17 eV)	1.40	1.539
BGE	1064 nm (1.27 eV)	0.80	0.503
BGE	1340 nm (0.93 eV)	1.55	1.886
BGE	1550 nm (0.93 eV)	1.10	0.951

REFERENCES

1. M. Wolf, “Limitation and possibilities for improvement of photovoltaic solar energy converts, part 1: considerations for earth’s surface operation,” Proc. IRE **48**, 1246-1263 (1960).
2. K. Bamham, G.Duggan, J. Appl. Phys. **67**, 3490 (1990).
3. A.Luque and A. Marti, Phys. Rev. Lett. **78**, 5014 (1997).
4. A.Luque, A. Mart, L. Cuadra, IEEE Trans. Electron Dev. **48**, 2118 (2001).
5. A.S. Brown, M.A. Green, R. P. Corkish, Physica E **14**, 121 (2002).
6. P.R. C. Kent and A. Zunger, Phys. Stat. Sol. (b) **228**, 253 (2001).
7. J. Václavík, D. Vápenka, EPJ Web of Conferences **48**, 00028 (2013).
8. P. P. Paskov, B. Monemar, Defects in Advanced Electronic Materials and Novel Low Dimensional Structures, Woodhead Publishing Series in Electronic and Optical Materials, Ch.2, Pages 27-61 (2018).
9. I. A. Buyanova, W. M. Chen, Defects in Advanced Electronic Materials and Novel Low Dimensional Structures, Woodhead Publishing Series in Electronic and Optical Materials, Ch. 7, Pages 189 (2018).
10. O. Y. Koval, V. V. Fedorov, N. V. Kryzhanovskaya, G. A. Sapunov, D. A. Kirilenko, E. V. Pirogov, N. G. Filosofov, A. Y. Serov, I. V. Shtrom, A. D. Bolshakov, and I. S. Mukhin, Cryst. Eng. Comm. **22**, 283 (2020).
11. S. Sukrittanon, Y. J. Kuang, A. Dobrovolsky, W. M. Kang, J. S. Jang, B. J. Kim, W. M. Chen, I. A. Buyanova, and C. W. Tu, Appl. Phys. Lett. **105**, 072107 (2014).
12. H. P. Xina and C. W. Tu, Y. Zhang and A. Mascarenhas, Appl. Phys. Lett. **76**, 10 (2000).
13. J. N. Baillargeon, K. Y. Cheng, G. E. Hofelr, P. J. Pearah, and K. C. Hsieh, Appl. Phys. Lett. **60**, 2540 (1992).
14. S. Sakai, Y. Uera and Y. Terauchi, J. Appl. Phys. **32**, 4413 (1993).
15. S. Miyoshi and K. Onabe, Solid-State Electron. **41**, 267 (1997).
16. L. Bellaiche, S. H. Wei, and A. Zunger, Phys. Rev. B **56**, 10233 (1997).
17. W. Shan, W. Walukiewicz, K. M. Yu, J. Wu, J. W. Ager III, E. E. Haller, H. P. Xin, and C. W. Tu, Appl. Phys. Lett. **76**, 3251 (2000).
18. Y. Zhang, B. Fluegel, A. Mascarenhas, H. P. Xin, and C. W. Tu, Phys. Rev. B **62**, 4493 (2000).
19. D. G. Thomas, J. J. Hopfield, and C. J. Frosch, Phys. Rev. Lett. **15**, 857 (1965).
20. D. G. Thomas and J. J. Hopfield, Phys. Rev. **150**, 680 (1966).
21. R. A. Logan, H. G. White, and W. Wiegman, Appl. Phys. Lett. **13**, 139 (1968).
22. W. O. Groves, A. H. Herzog, and M. G. Craford, Appl. Phys. Lett. **19**, 184 (1971).

23. E. Cánovas, A. Martí, A. Luque, and W. Walukiewicz: Appl. Phys. Lett. **93**, 174109 (2008).
24. H. B. Bebband, E. W. Williams, Semiconductors and Semimetals, Vol. 8 (Academic Press, New York), Chap. 5 (1972).
25. E. Calleja, F. J. Sanchez, D. Basak, M. A. Sánchez-García, E. Muñoz, I. Izpura, F. Calle, J. M. G. Tijero, J. L. Sánchez Rojas, B. Beaumont, P. Lorenzini, and P. Gibart, Phys. Rev. B **55**, 4689 (1997).
26. J. W. Kim, G. H. Song, and J. W. Lee, Appl. Phys. Lett. **88**, 182103 (2006).
27. A. Armstrong, M. H. Crawford, and D. D. Koleske, Appl. Phys. Express **7**, 032101 (2014).
28. M. Kaneko, T. Hashizume, V. A. Odnoblyudov, and C. W. Tu, J. Appl. Phys. **101**, 103707 (2007).
29. H. Jussila, K. M. Yu, J. Kujala, F. Tuomisto, S. Nagarajan, J. Lemettinen, T. Huhtio, T. O. Tuomi, H. Lipsanen, and M. Sopanen, J. Phys. D: Appl. Phys. **47**, 075106 (2014).
30. I. A. Buyanova, G. Yu. Rudko, W. M. Chen, H. P. Xin, and C. W. Tu: Appl. Phys. Lett. **80**, 1740 (2002).
31. M. D. Sturge, E. Cohen, and K. F. Rodgers: Phys. Rev. B **15**, 3169 (1977).
32. X. Zhang, K. Dou, Q.Hong and M. Balkanski: Phys. Rev. B **41**, 1376 (1990).
33. H. Yaguchi, G. Biwa, S. Miyoshi, D. Aoki, K. Arimoto, K. Onabe, R. Ito, and Y. Shiraki, J. of Cryst. Growth **189**, 496 (1998).
34. H Jussila, K M Yu, J Kujala, F Tuomisto, S Nagarajan, J Lemettinen, T Huhtio, T O Tuomi, H Lipsanen, and M Sopanen, J. Phys. D: Appl. Phys. **47**, 075106 (2014).
35. M. Wełna, K. Żelazna, A. Létoublon, C. Cornet, R. Kudrawiec, Solar Energy Materials and Solar Cells **196**, 131 (2019).
36. H. Yaguchi, S. Miyoshi, H. Arimoto, S. Saito, H. Akiyama, K. Onabe, Y. Shiraki, And R. Ito, Solid-State Electronics **41**, 231 (1997).
37. I. A. Buyanova, G. Pozina, J. P. Bergman, W. M. Chen, H. P. Xin, and C. W. Tu: Appl. Phys. Lett. **81**, 52 (2002).
38. Lu Yi-Jun, GAO Yu-Lin, ZHENG Jian-Sheng, ZHANG Yong, MASCARENHAS A, XIN H. P., and TU C. W., Chin. Phys. Lett. **11**, 2957 (2005).
39. S. Chen, W. M. Chen, and I. A. Buyanova, J. Phys. Chem. C **122**, 19212 (2018).
40. J. I. Pankove, Optical Processes in Semiconductors (Dover Publications, Inc., New York), page 61 and 107 (1971).
41. H. Yaguchi, J. Cryst. Growth **189**/**190**, 500 (1998).
42. I. A. Buyanova, M. Izadifard, A. Kasic, H. Arwin, W. M. Chen, H. P. Xin, Y. G. Hong, and C. W. Tu, Analysis of band anticrossing in $GaP_{1-x}N_x$ alloys, Phys. Rev. B **70**, 085209 (2004).

43. S. Miyoshi, H. Yaguchi, G. Biwa, K. Onabe, Y. Shiraki , and R. Ito, J. of Cryst. Growth **170**, 353 (1997).

44. H. Yaguchi, S. Miyoshi, M. Kibune, K. Onabe, R. Ito, and Y. Shiraki , J. of Cryst. Growth **145**, 87 (1994).

45. M. A. Greeen, Third generation photovoltaics: Ultra-high conversion efficiency at lowcost, Prog. Photovoltaics: Research and Application **9**, page 123-135 (2001).

46. R. Strandberg and T. W. Reenaas, Photofilling of intermediate bands, J. Appl. Phys. **105**, 12451 (2009).

47. Goldbery Yu.A. Handbook Series on Semiconductor Parameters, vol.1, World Scientific, London, page 104 (1996).

48. S. Miyoshi, H. Yaguchi, K. Onabe, R. Ito, and Y. Shiraki, Appl. Phys. Lett. **63**, 3506 (1994).

49. Tsukasa Hanaoka: "Study on High Energy Band of GaPN Alloy", Master's thesis, Saitama University (2013).

50. W. Shockley and W. T. Read, Phys. Rev. **87**, 835 (1952).

51. R. N. Hall, Electron-hole recombination in Germanium, Phys. Rev. **87**, 387 (1952).

52. H. G. Grirnmeiss, and B. Monemar, physica status solidi(a) **19**, 505 (1973).

53. M. Tajima, in 13th International Conference on Defects in Semiconductors, Coronado, California: The Metallurgical Society of AIME, (1984).

54. N. Kamata, E. Kanoh, T. Ohsaki, K. Yamada, Materials Science Forum **117-118**, 345 (1993).

55. J.M. Zanardi Ocampo, N. Kamata, K. Hoshino, K. Endoh, K. Yamada, M. Nishioka, T. Someya, Y. Arakawa, J. of Luminescence **87-89**, 363 (2000).

56. J.M. Zanardi Ocampo, H. Klausing, O. Semchinova, J. Stemmer, M. Hirasawa, N. Kamata, and K. Yamada, Phys. Stat. sol. (a) **183**, 189 (2001).

57. A. Z. M. Touhidul Islam, T. Hanaoka, K. Onabe, S. Yagi, N. Kamata, and H. Yaguchi, Appl. Phys. Express **6**, 0924 (2013).

58. T. Li, N. Kamata, Y. Kotsuka, T. Fukuda, Z. Honda, and T. Kurushima, Materials Letters **145**, 158 (2015).

59. E. Kanoh, K. Hoshino, N. Kamata, K. Yamada, M. Nishioka, and Y. Arakawa, J. Lumin **63**, 235 (1995).

60. N. Kamata, J. M. Z. Ocampo, K. Hoshino, K. Yamada, M. Nishioka, T. Someya, and Y. Arakawa, Recent Res. Dev. Quantum Electron. **1**, 123 (1999).

61. L. N. Dvoretckaia, A. D. Bolshakov, A. M. Mozharov, M. S. Sobolev, D. A. Kirilenko, A. I. Baranov, V. Yu Mikhailovskii, V. V. Neplokh, I. A. Morozov, V. V. Fedorov, I. S. Mukhin, Solar Energy Materials and Solar Cells **206**, 110282 (2020).

62. N. Kamata, M. Suetsugu, D. Haque, S. Yagi, H. Yaguchi, F. Karlsson, and Per-Olof Holz, Phys. Stat. Sol. B **254**, 1600566 (2017).

63. C. Negishi, Md D. Haque, N. Kamata, Z. Honda, and H. Yaguchi, Int. Workshop on Nitride Semiconductors, MoP-CR-10, Kanazawa, (2018).
64. S. Patel, N. Kamata, E. Kanoh and K. Yamada, Jpn. J. Appl. Phys **30**, L914 (1991).
65. N. Kamata, Phys. Status Solidi B **258**, 2000370 (2021).
66. Q. Dai, M. F. Schubert, M. H. Kim, J. K. Kim, E. F. Schubert, D. D. Koleske, M. H. Crawford, S. R. Lee, A. J. Fischer, G. Thaler, and M. A. Banas, Appl. Phys. Lett. **94**, 111109 (2009).
67. Y. S. Yoo, T. M. Roh, J. H. Na, S. J. Son, and Y. H. Cho, Appl. Phys. Lett. **102**, 211107 (2013).
68. P. Lu, D. Li, P. Zhang, D. Tan, W. Mu, J. Xu, W. Li and K. Chen, Optical Materials Express **6**, 3233 (2016).
69. L. Wu and G. R. Lin, IEEE J. Sel. Top. Quant. **19**, 3000109 (2013).
70. C. L. Wu and G. R. Lin, AIP Adv. **2**, 042162 (2012).
71. S. Miyoshi, H. Yaguchi, K. Onabe, and R. Ito and Y. Shiraki, Appl. Phys. Lett. **63**, 3506 (1993).
72. X. Liu, S. G. Bishop, J. N. Baillargeon, and K. Y. Cheng, Appl. Phys. Lett. **63**, 208 (1993).
73. K. Onabe, in MRS Symposium Proceedings edited by F. A. Ponce, T. D. Moustakas, I. Akasaki, and B. Monemar, Materials Research Society, Pittsburgh, 449, 23 (1997).
74. R. Kuroiwa, H. Asahi, K. Iwata, H. Tampo, K. Asami, and S. Gonda, Phys. Stat. Sol. B **216**, 461 (1999).